Theory of the charge density wave in math xmlns="http://www.w3.org/1998/Math/MathML">mrow>mi>A/mi>msub>mi mathvariant="normal">V/mi>mn>3/mn>/msub>msub>mi>Sb/mi>mn>5/mn>/msub>/mrow>/math> kagome metals

Morten H. Christensen, Turan Birol, Brian M. Andersen, and Rafael M. Fernandes

Theory of the charge-density wave in $A\mathrm{V_3Sb_5}$ kagome metals

Morten H. Christensen,[1, *] Turan Birol,[2] Brian M. Andersen,[1] and Rafael M. Fernandes[3]

[1]*Niels Bohr Institute, University of Copenhagen, 2100 Copenhagen, Denmark*
[2]*Department of Chemical Engineering and Materials Science, University of Minnesota, MN 55455, USA*
[3]*School of Physics and Astronomy, University of Minnesota, Minneapolis, MN 55455, USA*
(Dated: October 19, 2021)

The family of metallic kagome compounds $A\mathrm{V_3Sb_5}$ (A=K, Rb, Cs) was recently discovered to exhibit both superconductivity and charge order. The nature of the charge-density wave (CDW) phase is presently unsettled, which complicates the interpretation of the superconducting ground state. In this paper, we use group-theory and density-functional theory (DFT) to derive and solve a phenomenological Landau model for this CDW state. The DFT results reveal three unstable phonon modes with the same in-plane momentum but different out-of-plane momenta, whose frequencies depend strongly on the electronic temperature. This is indicative of an electronically-driven CDW, stabilized by features of the in-plane electronic dispersion. Motivated by the DFT analysis, we construct a Landau free-energy expansion for coupled CDW order parameters with wave-vectors at the M and L points of the hexagonal Brillouin zone. We find an unusual trilinear term coupling these different order parameters, which can promote the simultaneous condensation of both CDWs even if the two modes are not nearly-degenerate. We classify the different types of coupled multi-$\mathbf{Q}$ CDW orders, focusing on those that break the sixfold rotational symmetry and lead to a unit-cell doubling along all three crystallographic directions, as suggested by experiments. We determine a region in parameter space, characterized by large nonlinear Landau coefficients, where these phases – dubbed staggered tri-hexagonal and staggered Star-of-David – are the leading instabilities of the system. Finally, we discuss the implications of our results for the kagome metals.

I. INTRODUCTION

The kagome lattice offers a powerful framework to investigate several intriguing physical phenomena, such as frustrated magnetism and spin liquids [1], flat bands [2–4], and Dirac points [5, 6]. An exotic chiral d-wave superconducting phase promoted by van Hove singularities has also been predicted for certain carrier concentrations [7–10], providing a possible route to realize an intrinsic topological superconductor. The synthesis and subsequent discovery of superconductivity in a family of metallic kagome compounds, $A\mathrm{V_3Sb_5}$ (A=K, Rb, Cs), provides the opportunity of potentially realizing this prediction in a real material [11–14]. The superconducting critical temperature varies between $T_c \sim 1-3$ K depending on the alkali metal and can be increased upon either hole doping [15] or application of pressure [16–20]. In addition, near $T_{\mathrm{CDW}} \sim 80-100$ K, these materials exhibit a kink in the specific heat [11] that has been widely interpreted as a signature of a charge-density wave (CDW) [11, 12, 14, 21–23]. This ordered state is also observed in scanning tunneling microscopy (STM) measurements at low temperatures, which report static charge modulations consistent with a doubling of the unit cell along both the a- and b-directions [23–26]. It is also supported by x-ray diffraction which, in addition to the doubling along the a- and b-directions, find a unit cell increase along the c-direction [23, 27, 28]. While some experiments report a simple doubling along the c-direction [25], corresponding to $2 \times 2 \times 2$ order, a recent work reported

a structure consistent with a $2 \times 2 \times 4$ increase of the unit cell [28]. Several spectroscopic probes have also reported evidence for the three-dimensionality of the CDW order [25, 29]. Finally, recent transport measurements under uniaxial strain indicates that the CDW state competes strongly with superconductivity [30].

The nature of the CDW state is currently under intense scrutiny. Since superconductivity sets in at much lower temperatures than charge order, elucidating the symmetries and properties of the CDW phase is essential to understand e.g. the symmetry of the superconducting order parameter. In this regard, while there is spectroscopic evidence for both Star-of-David and tri-hexagonal (also known as inverse Star-of-David) configurations in the plane [23, 24, 31] (see Fig. 1), the character of the interlayer modulation responsible for the unit-cell doubling along the c-direction remains under debate. The observation of threefold rotational symmetry-breaking by STM experiments [23, 24, 26, 31] offers important clues about the three-dimensional character of the CDW pattern. In particular, recent density functional theory (DFT) calculations [32] and coherent phonon spectroscopy [33] suggest that the system has unstable phonon modes at both the M and L points of the hexagonal Brillouin zone [BZ, illustrated in Fig. 1(a)]. Under these conditions, the only way to obtain a charge-ordered state that doubles the unit cell in every direction *and* lowers the sixfold rotational symmetry to twofold is by a combination of wave-vectors from both the M and L points. Indeed, DFT analyses find that the energy of the system is minimized by a configuration that intertwines wave-vectors from both the M and L points [32, 33]. We note that STM data has also been interpreted in terms of a chiral charge

* mchriste@nbi.ku.dk

order [23, 34–37] whereas μSR experiments have been interpreted in favor of time-reversal symmetry-breaking associated with orbital currents in the CDW state [38].

The condensation of CDW order parameters associated with two different BZ momenta, M and L, which is necessary to explain the $2 \times 2 \times 2$ unit-cell expansion and the breaking of sixfold rotational symmetry, raises several important questions. Why would two different types of CDW order condense? Do the two order parameters onset simultaneously or at two different temperatures? What is the mechanism responsible for the intertwining of these CDW orders? In this paper, we employ a phenomenological approach, combined with DFT calculations, to address these issues. Our DFT analysis reveals a strong dependence of the unstable M and L phonon frequencies on Fermi surface smearing – a proxy of the electronic temperature – which is indicative of an electronic rather than a structural mechanism for the formation of the charge order. We also find another unstable mode along the U-line connecting the M and L momenta of the BZ, see Fig. 1(a). The fact that three charge-order configurations with different c-axis periodicity but identical in-plane periodicity are viable instabilities suggests that the electronic mechanism is dominated by in-plane processes. Such a mechanism could be connected, for example, to the van Hove singularities of the in-plane electronic dispersion of the kagome lattice, as found by a recent renormalization group calculation [39].

For the phenomenological analysis, we write down and minimize the most general Landau free-energy expansion for the CDW order parameters associated with the M and L wave-vectors. Generally, we find that a direct transition to a coupled M-L state requires a trilinear coupling that compensates the energy difference between the two "pure" states. This opens the possibility of a coupled state appearing even if the "pure" instabilities are not nearly-degenerate. Over a wide range of parameters, the leading coupled-state instability is the superimposed tri-hexagonal Star-of-David charge order, which corresponds to a triple-$\mathbf{Q}_M$/triple-$\mathbf{Q}_L$ order that does not break sixfold rotational symmetry. The latter is broken by the single-$\mathbf{Q}_M$/double-$\mathbf{Q}_L$ orders dubbed staggered tri-hexagonal and staggered Star-of-David orders. These orders are illustrated in Fig. 6. For most of the parameter space analyzed here, these two states are not the leading instabilities of the system, but onset at temperatures below the superimposed tri-hexagonal Star-of-David order or below the pure triple-$\mathbf{Q}_M$ planar Star-of-David (or planar tri-hexagonal, see Fig. 4) order. Only when the nonlinear quartic terms are large enough we find a direct, single phase transition to the single-$\mathbf{Q}_M$/double-$\mathbf{Q}_L$ orders that break sixfold rotational symmetry. Our results point to the key role played by the nonlinear couplings between the M and L CDWs in the AV$_3$Sb$_5$ kagome metals, and call for further experimental studies to determine whether a single or multiple charge-order transitions are realized in these compounds.

The paper is organized as follows: We present our DFT analysis in Sec. II, and in Sec. III we introduce and motivate the Landau free energy describing a system of coupled CDW orders. The uncoupled free energies are minimized in Secs. III A and III B. In Sec. IV we minimize the fully coupled free energy and elucidate the various phases that emerge. Sec. V is devoted to the conclusions.

II. PHONON INSTABILITIES IN AV$_3$Sb$_5$: DFT AND SYMMETRY ANALYSIS

We start by identifying the unstable lattice modes associated with the CDW transition. We performed lattice response calculations in CsV$_3$Sb$_5$ using DFT as implemented in the Vienna Ab Initio Simulation package [40–42]. We employed the Perdew-Burke-Ernzerhof exchange correlation functional for the solids (PBEsol) [43], and used unshifted k-grids with a density of a point per $\sim 0.012 \times 2\pi \text{Å}^{-1}$. The plane wave energy cutoff was set to 350 eV and a Gaussian smearing scheme was used for the electronic occupations. The phonon frequencies were calculated using the frozen phonons (direct) approach, which involves displacing atoms one by one and performing single shot DFT calculations to obtain the forces and build the dynamical matrix.

In agreement with earlier results in the literature [33], our DFT calculations find two unstable phonon modes that transform as the M_1^+ and L_2^- irreducible representations (irreps) of the space group $P6/mmm$ (#191). Formally, M_1^+ and L_2^- are one-dimensional irreps of the little group of the wave-vectors M and L. However, there are three vectors in the stars of both the M and L points, as shown in Fig. 1(a). The vectors in the star of M are

$$\mathbf{Q}_M^{(1)} = (\tfrac{1}{2}\ 0\ 0)\,,\ \mathbf{Q}_M^{(2)} = (0\ \tfrac{1}{2}\ 0)\,,\ \mathbf{Q}_M^{(3)} = (-\tfrac{1}{2}\ -\tfrac{1}{2}\ 0)\,, \tag{1}$$

and those in the star of L are

$$\mathbf{Q}_L^{(1)} = (\tfrac{1}{2}\ 0\ \tfrac{1}{2})\,,\ \mathbf{Q}_L^{(2)} = (0\ \tfrac{1}{2}\ \tfrac{1}{2})\,,\ \mathbf{Q}_L^{(3)} = (-\tfrac{1}{2}\ -\tfrac{1}{2}\ \tfrac{1}{2})\,, \tag{2}$$

in the basis $(\mathbf{G}_1, \mathbf{G}_2, \mathbf{G}_3)$ with

$$\mathbf{G}_1 = \frac{2\pi}{a} \begin{pmatrix} 1 \\ \frac{1}{\sqrt{3}} \\ 0 \end{pmatrix}, \ \mathbf{G}_2 = \frac{2\pi}{a} \begin{pmatrix} 0 \\ \frac{2}{\sqrt{3}} \\ 0 \end{pmatrix}, \ \mathbf{G}_3 = \frac{2\pi}{c} \begin{pmatrix} 0 \\ 0 \\ 1 \end{pmatrix}. \tag{3}$$

Hence, for the M_1^+ irrep, we denote the components of the CDW order parameter with different wave-vectors in the star by M_i, which corresponds to a displacement with wave-vector $\mathbf{Q}_M^{(i)}$ ($i = 1, 2, 3$). A similar notation is defined for L_i and $\mathbf{Q}_L^{(i)}$.

In real space, the in-plane displacements of the V atoms, see Figs. 1(b) and 1(c), account for more than 90% of the total displacements associated with the M and L modes. The only significant difference between them is in the relative phase of the displacements in neighboring V layers along the c direction. For the M mode, the
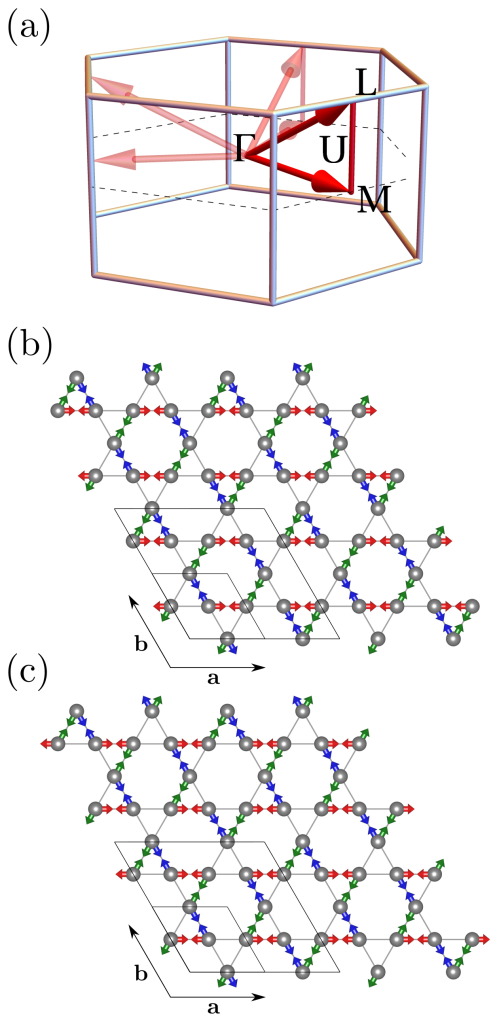
Figure 1. (a) Illustration of the three-dimensional hexagonal Brillouin zone (BZ) corresponding to the space group $P6/mmm$ with the M and L points highlighted, as well as the U line connecting them. The other two wave-vectors in the stars of M and L are obtained by three-fold rotations. (b)-(c) The displacement pattern of the V ions on a kagome layer according to the unstable M_1^+ and L_2^- modes. Both of these modes lead to similar distortions on a single kagome layer. Different components (M_1, M_2, and M_3) are shown with arrows of different colors. Here (b) corresponds to the bond displacements of the tri-hexagonal charge order, described by $|M_1| = |M_2| = |M_3|$ and $M_1 M_2 M_3 > 0$. In (c) the bond displacements that give rise to the Star-of-David order are shown. In this case, $|M_1| = |M_2| = |M_3|$ but $M_1 M_2 M_3 < 0$.

V atoms are displaced in-phase between the layers, while for the L mode, the displacement is out-of-phase between the layers.

Figs. 1(b) and 1(c) show the in-plane displacement patterns of the V atoms corresponding to the three wave-vectors of the star of either the M or the L point. The red, green, and blue displacement patterns denote different periodicities corresponding to each of the three

distinct order parameters M_i (or L_i). Note that the predominant displacement is a shortening of certain nearest neighbor V–V bonds. As a result, we associate the CDW ordered states to a pattern of shorter V–V bonds, i.e. a bond-order pattern.

For an isolated layer, the equal-weight superposition of the three types of in-plane bond-order can give rise to two distinct sixfold-symmetric patterns. If all V–V bond displacements have the same phase, or more generally for any ground state with $|M_1| = |M_2| = |M_3|$ and $M_1 M_2 M_3 > 0$, the resulting pattern is the tri-hexagonal (or inverse Star-of-David) bond-order configuration shown in Fig. 1(b). In this state, there are short and long V–V bond-loops forming triangles and hexagons. On the other hand, if we shift the phase of one of the three bond displacements by π, or more generally for any ground state with $|M_1| = |M_2| = |M_3|$ and $M_1 M_2 M_3 < 0$, the resulting configuration is the so-called Star-of-David bond-order pattern of Fig. 1(c). In this state, twelve V atoms form a bond-loop in the shape of a six-pointed star. We note that even though the Star-of-David and the inverse Star-of-David phases have different bond-order patterns, these phases break the same symmetries of the high temperature structure. In other words, their space groups and unit cells are identical.

Going beyond an isolated layer, the bond pattern in consecutive layers depends on whether the wave-vector is in the star of M or L. In the former case, the triple-$\mathbf{Q}_M$ bond patterns of Figs. 1(b)-(c) are the same for all layers. We refer to these two different states as planar tri-hexagonal and planar Star-of-David, respectively. On the other hand, in the case of a triple-$\mathbf{Q}_L$ bond-order, consecutive layers will alternate between the tri-hexagonal and Star-of-David patterns, regardless of the relative phases between the L_i order parameters. Therefore, there is only one triple-$\mathbf{Q}_L$ state that we dub alternating tri-hexagonal Star-of-David state (see Fig. 4). We will further discuss this type of bond-order in Sec. III B. Note that any combination of the order parameters M_i can be represented in terms of a $2 \times 2 \times 1$ supercell, which is shown in the lower left corner of Fig. 1(b), whereas combinations of L_i require a $2 \times 2 \times 2$ supercell.

While no phonon instabilities have been reported at other high symmetry points of the BZ, our DFT calculations also found an instability on the U line that connects the M and L points [see Fig. 1(a)]. A point on this line is parametrized by $\mathbf{Q}_U^{(3)} = (-\frac{1}{2} \ -\frac{1}{2} \ q_z)$ (and its three-fold symmetric partners), with $q_z = 0$ corresponding to the M point and $q_z = \frac{1}{2}$, to the L point. The corresponding bond-order patterns are generally incommensurate along the c-axis. For our DFT calculations, we considered the commensurate case $q_z = \frac{1}{4}$, resulting in a CDW state with a $2 \times 2 \times 4$ unit cell. It is interesting to note that such a periodicity has been proposed in recent experiments [28]. The fact that the three instabilities uncovered here have the same in-plane wave-vector suggests that the driving force behind them are not the phonons themselves, but their interaction with
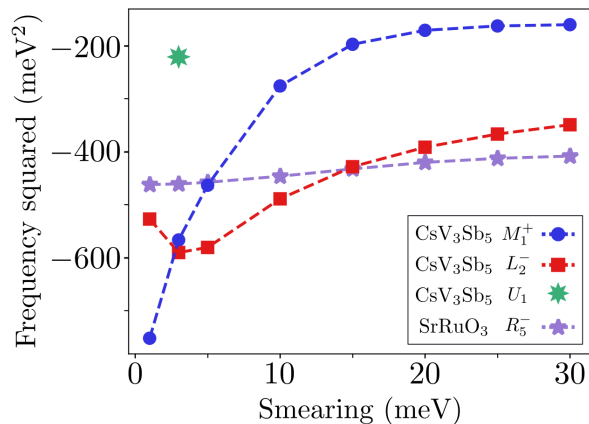
Figure 2. Squared frequency of the unstable phonon modes of CsV_3Sb_5 and $SrRuO_3$ as a function of Fermi surface smearing (in meV), which is a proxy for the electronic temperature. For the kagome material CsV_3Sb_5, there is a significant change of the frequency as the electronic temperature increases. In contrast, for $SrRuO_3$, which also shows a structural instability with a condensation of the R_5^- phonon mode, the frequency depends very weakly on electronic smearing. Taken together, we interpret these results as indicating that the electronic degrees of freedom play an important role in driving the structural transition in CsV_3Sb_5.

the electronic degrees of freedom – and, in particular, the in-plane electronic dispersion, which may display van Hove singularities [28, 44–46]. This is supported by the fact that the displacements associated with the M and L phonon modes occur primarily on the V atoms, which are the dominant contributors to the density of states at the Fermi level.

To further examine the effects of the electronic degrees of freedom on the lattice instabilities, we repeat our DFT calculations as a function of Fermi surface smearing. Fermi-surface induced lattice instabilities depend sensitively on the electronic temperature of the system. While the DFT calculations are in principle performed at zero temperature, it is possible to consider Fermi surface smearing when calculating the occupations of the electronic energy levels. We employ a Gaussian smearing scheme, where the occupation probability of a state depends on a Gaussian function of its energy with respect to the Fermi level. The width of this Gaussian, σ, is a proxy for the electronic temperature. Consequently, electronically-driven instabilities are expected to weaken or disappear as σ is increased.

To assess the evolution of the strength of phonon instabilities as the electronic temperature is changed, in Fig. 2 we present the square of the M_1^+ and L_2^- phonon frequencies as function of the smearing width σ. Because unstable phonon modes have imaginary-valued frequencies, the smaller the absolute value of the squared frequency is, the weaker the corresponding instability is expected to be. Consistent with an instability for which the electrons play a substantial role, the absolute value of the squared
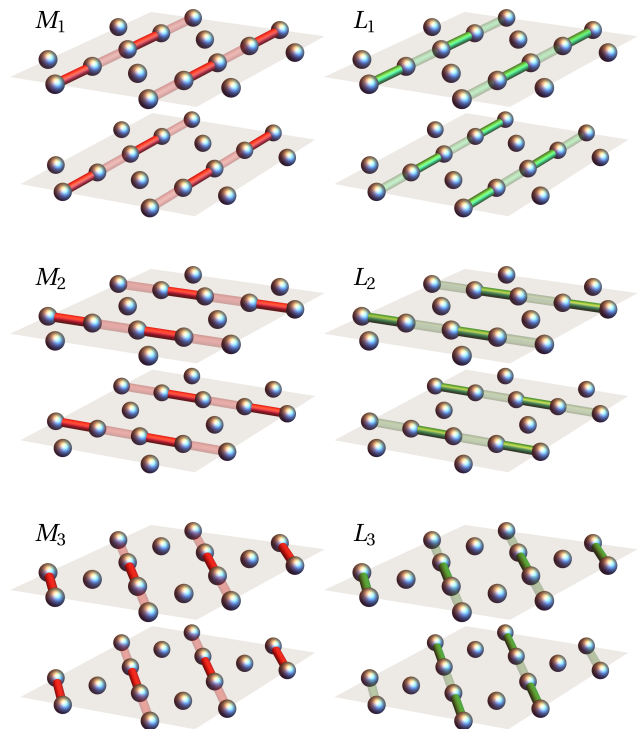

Figure 3. Bond-order configurations corresponding to the order parameters M_i and L_i. We use the notation $\overline{M}_i \equiv -M_i$ and $\overline{L}_i \equiv -L_i$ to refer to the configurations in which the strong and weak bonds are interchanged.

frequencies of the unstable phonon modes decrease significantly when the electronic temperature is increased, particularly for the M_1^+ mode. In the same plot, the unstable U_1 phonon mode, which was computed for a single smearing value, is shown by the green symbol. As a comparison, we also plot the squared frequency of the unstable phonon mode (labeled R_5^-) of the metallic compound $SrRuO_3$ as a function of Fermi-surface smearing. In this case, where the phonon instability is not related to a Fermi-surface effect, the frequencies barely change as the electronic temperature increases.

III. LANDAU FREE-ENERGY EXPANSION FOR CDW ORDER

To elucidate the possible CDW instabilities of the system with unstable M_1^+ and L_2^- phonon modes, we derive the Landau free-energy expansion for the coupled M_i and L_i order parameters, with $i = 1, 2, 3$. For our phenomenological treatment, it is unimportant whether M_i and L_i are lattice distortions or electronic CDWs, since all of these orders transform as the same irreducible representations of the space group. The important point is that each component of these order parameters has a different wave-vector, since they come from different symmetry-equivalent points in the star of the M and L points of the BZ. As stated above, the wave-vector of M_i

is $\mathbf{Q}_M^{(i)}$ whereas L_i has wave-vector $\mathbf{Q}_L^{(i)}$ [see Eqs. (1) and (2)]. In Fig. 3, we represent each of the three components of these order parameters separately as bond-order patterns in two consecutive layers. Clearly, each M_i or L_i component corresponds to a stripe pattern of bond order that doubles the unit cell along the stripe direction. In the case of the L_i order parameter, the unit cell is also doubled along the c-axis.

We use the INVARIANTS tool [47] to scan all combinations of M_i and L_i that transform trivially under the space group, up to quartic order in the order parameters. We obtain the Landau free-energy:

$$\mathcal{F}_{\text{tot}} = \mathcal{F}_M + \mathcal{F}_L + \mathcal{F}_{ML}, \qquad (4)$$

$$\mathcal{F}_M = \frac{\alpha_M}{2} M^2 + \frac{\gamma_M}{3} M_1 M_2 M_3 \qquad (5)$$
$$+ \frac{u_M}{4} M^4 + \frac{\lambda_M}{4} \left(M_1^2 M_2^2 + M_1^2 M_3^2 + M_2^2 M_3^2 \right),$$

$$\mathcal{F}_L = \frac{\alpha_L}{2} L^2 + \frac{u_L}{4} L^4 \qquad (6)$$
$$+ \frac{\lambda_L}{4} \left(L_1^2 L_2^2 + L_1^2 L_3^2 + L_2^2 L_3^2 \right),$$

$$\mathcal{F}_{ML} = \frac{\gamma_{ML}}{3} \left(M_1 L_2 L_3 + L_1 M_2 L_3 + L_1 L_2 M_3 \right) \qquad (7)$$
$$+ \frac{\lambda_{ML}^{(1)}}{4} \left(M_1 M_2 L_1 L_2 + M_1 M_3 L_1 L_3 + M_2 M_3 L_2 L_3 \right)$$
$$+ \frac{\lambda_{ML}^{(2)}}{4} \left(M_1^2 L_1^2 + M_2^2 L_2^2 + M_3^2 L_3^2 \right) + \frac{\lambda_{ML}^{(3)}}{4} M^2 L^2,$$

where, e.g., $M^2 = M_1^2 + M_2^2 + M_3^2$ and $M^4 = (M^2)^2$. As M_i and L_i belong to different irreducible representations, α_M and α_L will in general be different, which in turn is manifested in different transition temperatures, at least in the absence of a coupling between the two. Thus, we will assume $\alpha_M = \alpha(T - T_M)$ and $\alpha_L = \alpha(T - T_L)$ and, in the numerical calculations presented in Sec. IV, we will set $\alpha = 1$.

Note the asymmetry between $\mathcal{F}_M$ and $\mathcal{F}_L$: while $\mathcal{F}_M$ has a trilinear term, $\mathcal{F}_L$ does not. This is a direct consequence of the different wave-vectors of the order parameters M_i and L_i described above, since $\sum_i \mathbf{Q}_M^{(i)} = 0$ but $\sum_i \mathbf{Q}_L^{(i)} \neq 0$. An uncommon feature of the free energy expansion in the equations above is the presence of a trilinear coupling γ_{ML} between components of two order parameters that transform as different irreps. While cubic terms involving the components of a single order parameter are rather common [48], for example in isostructural transitions or in a transition described by the four-state clock model, trilinear terms involving different order parameters are rare. The closest example to the free energy expansion discussed in this study is possibly observed in the layered perovskite ferroelectrics where there are trilinear couplings between two octahedral rotation modes and the electrostatic polarization [49, 50]. In that case, these couplings were shown to give rise to different types of phase transitions; for instance, a large enough trilinear coupling by itself could induce a first-order transition where multiple order parameters condense simulta-
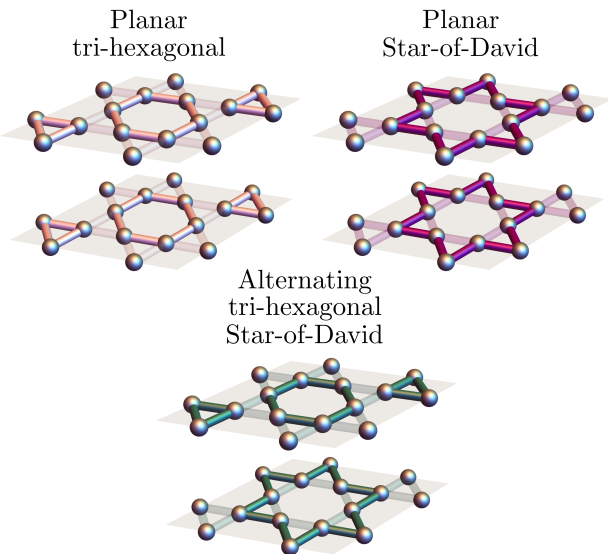

Planar tri-hexagonal

Planar Star-of-David

Alternating tri-hexagonal Star-of-David

Figure 4. Triple-$\mathbf{Q}$ bond-order configurations obtained from minimizing the uncoupled free energies $\mathcal{F}_M$ or $\mathcal{F}_L$. The upper panels correspond to the two types of triple-$\mathbf{Q}_M$ order, whereas the lower panel illustrated the triple-$\mathbf{Q}_L$ order. They correspond to linear combinations of the three M_i or three L_i shown in Fig. 3, as explained in Table I.

neously [51]. We will argue in Sec. IV that a similar phenomenon may occur in the CDW kagome metals. In particular, the trilinear term with coefficient γ_{ML} promotes phases in which both M_i and L_i are finite, playing a leading role in shaping the phase diagram.

In the remainder of this section, we restrict our analysis to the two terms $\mathcal{F}_M$ and $\mathcal{F}_L$, which are considered separately. In Sec. IV we tackle the full free-energy for the coupled CDW order parameters. The possible minima of $\mathcal{F}_M$ and $\mathcal{F}_L$ that will be derived below are summarized in Table I, and schematically illustrated in Figs. 3 and 4.

A. CDW order at the M point

We start by analyzing the case where only the M_i CDW order parameters are allowed to condense. The trilinear term in $\mathcal{F}_M$ in Eq. (5) plays a primary role in selecting the leading instability. Since the individual M_i can always be chosen in a configuration for which the contribution from the trilinear term to the free energy is negative, regardless of the sign of γ_M, this term will always lower the energy of the triple-$\mathbf{Q}_M$ configuration, in which all $|M_i| = M$. For $\gamma_M < 0$, the bond-order configuration corresponds to the planar tri-hexagonal of Fig. 4, with $\text{sign}(M_1 M_2 M_3) > 0$, whereas for $\gamma_M > 0$, it corresponds to the planar Star-of-David of Fig. 4, with $\text{sign}(M_1 M_2 M_3) < 0$. Importantly, the trilinear term contribution vanishes for the single-$\mathbf{Q}_M$ stripe configurations of Fig. 3, where only one M_i is non-zero in the CDW phase. Hence, a triple-$\mathbf{Q}_M$ phase will always be favored,

Phase	Color	$\mathbf{Q}$-vector	OP	Unit cell	C_6	Space group
Planar stripe		$\mathbf{Q}_M$	$(M00)$	2×1×1	No	$Pmmm$ (#47)
Planar tri-hexagonal		$3\mathbf{Q}_M$	(MMM)	2×2×1	Yes	$P6/mmm$ (#191)
Planar Star-of-David		$3\mathbf{Q}_M$	$(\overline{M}MM)$	2×2×1	Yes	$P6/mmm$ (#191)
Alternating stripe		$\mathbf{Q}_L$	$(L00)$	2×1×2	No	$Immm$ (#71)
Alternating tri-hexagonal Star-of-David		$3\mathbf{Q}_L$	(LLL)	2×2×2	Yes	$P6/mmm$ (#191)

Table I. Summary of the phases that minimize the uncoupled free energies $\mathcal{F}_M$ or $\mathcal{F}_L$. The single-$\mathbf{Q}$ stripe phases are illustrated in Fig. 3 whereas the triple-$\mathbf{Q}$ phases are shown in Fig. 4. The order parameter (OP) column refers to the type of order parameters $(M_1M_2M_3)$ and $(L_1L_2L_3)$ that are condensed in the corresponding phase. For instance, in the planar Star-of-David phase, all three M_i are finite and identical in magnitude, but one has the opposite sign of the other two. In the fifth column we report the increase in the unit cell brought on by the condensation of the respective phase. This is reported relative to the disordered phase. The sixth column denotes whether the associated phase respects six-fold rotational symmetry (C_6), and the seventh column displays the space group of the ordered CDW phase. Even though there are multiple phases which have the same space group as the parent structure ($P6/mmm$), these phases have larger unit cells and hence lower translational symmetry.

no matter the sign of λ_M.

To derive these results, we start by calculating the value of the free energy in the triple-$\mathbf{Q}_M$ phase:

$$\mathcal{F}_M^{3Q} = \frac{\mathcal{K}^2}{2592u_{M*}^3}\left[54\alpha(T-T_M)u_{M*} - |\gamma_M|\mathcal{K}\right],\quad (8)$$

where

$$u_{M*} = 3u_M + \lambda_M,\quad (9)$$

$$\mathcal{K} = |\gamma_M| + \sqrt{\gamma_M^2 - 36\alpha(T-T_M)u_{M*}},\quad (10)$$

Note that, for the free energy to remain bounded, we must require $u_{M*} > 0$. For the single-$\mathbf{Q}_M$ phase, the free energy is given by:

$$\mathcal{F}_M^{1Q} = -\frac{\alpha^2(T-T_M)^2}{4u_M},\quad (11)$$

Therefore, in addition to $u_{M*} > 0$, we must also require that $u_M > 0$ for the free energy to remain bounded. While $\mathcal{F}_M^{1Q}$ crosses zero at $T = T_M$, $\mathcal{F}_M^{3Q}$ does so at

$$T_M^{3Q} = \frac{2\gamma_M^2}{81\alpha u_{M*}} + T_M,\quad (12)$$

which is always larger than T_M if the free energy is bounded and the trilinear coefficient γ_M is not zero. Hence, the trilinear term induces a transition to a triple-$\mathbf{Q}_M$ phase. The order parameters are given by:

$$M_i = \pm\frac{\mathcal{K}}{6u_{M*}},\quad (13)$$

with the relative signs chosen such that $\mathrm{sgn}(\gamma_M M_1 M_2 M_3) < 0$. Thus, at the transition to the triple-$\mathbf{Q}_M$ phase, the order parameter exhibits a jump proportional to γ_M:

$$|\Delta M_i| = \frac{2|\gamma_M|}{9u_{M*}}.\quad (14)$$

The triple-$\mathbf{Q}_M$ phase in which $\mathrm{sgn}(M_1M_2M_3) > 0$ takes place for $\gamma_M < 0$ and corresponds to the planar tri-hexagonal phase (see Table I and Fig. 4). There are four equivalent ground states corresponding to four different ways of arranging the enhanced $2 \times 2 \times 1$ unit cell, given by the combinations of order parameters $(M_1M_2M_3) = (MMM), (M\overline{M}\overline{M}), (\overline{M}M\overline{M})$, and $(\overline{M}\overline{M}M)$. Here, we denote $\overline{M}_i \equiv -M_i$. Analogously, for $\gamma_M > 0$, the resulting configuration is the planar Star-of-David phase shown in Fig. 4. It is characterized by $\mathrm{sgn}(M_1M_2M_3) < 0$ and consists of four equivalent states $(M_1M_2M_3) = (MM\overline{M}), (M\overline{M}M), (\overline{M}MM)$, and $(\overline{M}\overline{M}\overline{M})$. The space group of both planar tri-hexagonal and planar Star-of-David phases is $P6/mmm$, which is the same as the space group of the compound without charge order.

These considerations are valid for the leading instability of $\mathcal{F}_M$ in Eq. (5). When the quartic coefficient $\lambda_M > 0$, however, the corresponding quartic term penalizes the triple-$\mathbf{Q}_M$ phase and vanishes for the single-$\mathbf{Q}_M$ phase. As a result, because the quartic term is sub-leading with respect to the cubic term, the single-$\mathbf{Q}_M$ phase corresponding to the in-plane stripes shown in Fig. 3 can occur for $\lambda_M > 0$ as a sub-leading instability that onsets at a temperature $T_M^Q < T_M^{3Q}$ given by:

$$T_M^Q = -\frac{\gamma_M^2}{9\alpha\lambda_M^2 u_{M*}}\Big[\sqrt{u_M(4u_M + \lambda_M)^3} + u_M(8u_M + 3\lambda_M)\Big] + T_M,\quad (15)$$

which, like the other quantities above, is independent of the sign of γ_M. This state has a three-fold degeneracy and is parametrized by $(M00), (0M0)$, and $(00M)$. It lowers the sixfold rotational symmetry to twofold, and has space group $Pmmm$. Note that, if $\lambda_M < 0$, the triple-$\mathbf{Q}_M$ phase is always favored over the single-$\mathbf{Q}_M$ stripe phase. The phase diagram for CDW order at the M point is shown in Fig. 5(a) (for $\lambda_M > 0$). The colors correspond to those shown in Table I. As expected, a double-$\mathbf{Q}_M$ phase is never favored.
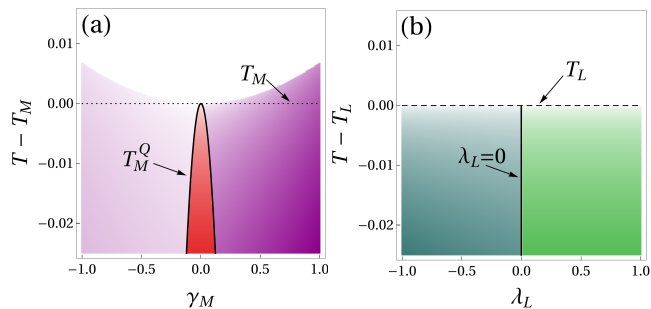
Figure 5. (a) Phase diagram for CDW order at the M point only, obtained from minimizing the free energy $\mathcal{F}_M$. Here, $\lambda_M = 0.6$ and $u_M = 1.0$. These values only affect the precise shape of the single-$\mathbf{Q}_M$ region [see Eq. (15)]. Colors correspond to the phases listed in Table I and illustrated in Figs. 3 and 4. As explained in the text, the leading instability is always to one of the two triple-$\mathbf{Q}_M$ phases. The sign of γ_M decides between the planar tri-hexagonal ($\gamma_M < 0$, light purple) and the planar Star-of-David ($\gamma_M > 0$, dark purple) phases. For positive λ_M, a secondary transition to a single-$\mathbf{Q}_M$ phase occurs at lower temperatures (red), although for $\gamma_M = 0$ this can occur at $T = T_M$. For negative λ_M, the triple-$\mathbf{Q}_M$ phase is always favored. The upwards curvature of the transition temperature is a consequence of the cubic term as discussed in the text [see Eq. (12)]. (b) Phase diagram for CDW order at the L point only, obtained from minimizing $\mathcal{F}_L$. Here, for concreteness, we chose $u_L = 1.0$, although it has no impact on the shape of the phase diagram. The sign of λ_L selects between the single-$\mathbf{Q}_L$ ($\lambda_L > 0$, green) and triple-$\mathbf{Q}_L$ ($\lambda_L < 0$, petroleum) phases. No secondary transitions occur at lower temperatures.

B. CDW order at the L point

We now proceed to analyze the free energy $\mathcal{F}_L$, which contains only the L_i order parameters. The absence of a cubic (trilinear) term makes the analysis simpler than the case of M_i. Specifically, the sign of the quartic coefficient λ_L completely determines whether the instability is towards the single-$\mathbf{Q}_L$ or the triple-$\mathbf{Q}_L$ phase. The former gives rise to the alternating pattern of stripes with opposite phases in consecutive layers shown in Fig. 3. As displayed in Table I, the space group of this alternating stripe CDW phase is $Immm$, which does not have C_6 rotational symmetry and is different from the space group of the single-$\mathbf{Q}_M$ planar stripe-phase.

As for the triple-$\mathbf{Q}_L$ phase, it consists of a bond-order configuration of alternating tri-hexagonal and Star-of-David patterns in consecutive layers, as shown in Fig. 4. In contrast to the case of CDW order at the M point, there is only a single eight-fold degenerate triple-$\mathbf{Q}_L$ phase, rather than two four-fold degenerate triple-$\mathbf{Q}_M$ phases. This is a consequence of the fact that the unit cell in the triple-$\mathbf{Q}_L$ phase is enhanced by a factor of eight. Consequently, the configurations (LLL) and $(\bar{L}LL)$ are related by translational symmetry and correspond to different "domains" of the same phase. Interestingly, as shown in Table I, the alternating tri-hexagonal Star-of-

David phase shares the same space group as the planar tri-hexagonal and planar Star-of-David CDW states, which preserves sixfold rotational symmetry.

Minimizing the free energy $\mathcal{F}_L$ in each of the two phases gives:

$$\mathcal{F}_L^{1Q} = -\frac{\alpha^2 (T - T_L)^2}{4u_L}, \qquad (16)$$

$$\mathcal{F}_L^{3Q} = -\frac{\alpha^2 (T - T_L)^2}{4u_L + \frac{4}{3}\lambda_L}. \qquad (17)$$

Thus, for the free energy to remain bounded, both $u_L > 0$ and $3u_L + \lambda_L > 0$. These are identical to the conditions for u_M and λ_M reported above. Comparison between $\mathcal{F}_L^{1Q}$ and $\mathcal{F}_L^{3Q}$ shows that a single-$\mathbf{Q}_L$ phase is favored for $\lambda_L > 0$ and a triple-$\mathbf{Q}_L$ phase is favored for $\lambda_L < 0$, as anticipated. The resulting phase diagram is shown in Fig. 5(b), with the colors corresponding to the CDW states outlined in Table I. As in the case of $\mathcal{F}_M$, a double-$\mathbf{Q}_L$ phase is not favored in any region of the phase diagram. In contrast to that case, however, no sub-leading instabilities appear in the phase diagram.

C. CDW order along the U line

While several experimental observations support a $2 \times 2 \times 2$ supercell for the CDW phase of CsV_3Sb_5, the possibility of a $2 \times 2 \times 4$ phase has been raised in Ref. 28. Combinations of the L_i and M_i order parameters cannot lead to a supercell with a periodicity of 4 lattice constants along the c direction. Instead, translational symmetry breaking that leads to a $2 \times 2 \times 4$, or in general $2 \times 2 \times n$ (where $n > 2$) unit cell, requires CDW order with wave-vectors on the U line of the Brillouin zone, which connects the M and L points. A generic wave-vector along this line has six vectors in its star, described by the inversion-symmetry-related pairs $\pm\mathbf{Q}_U^{(1)} = \pm(\frac{1}{2} \, 0 \, q_z)$, $\pm\mathbf{Q}_U^{(2)} = \pm(0 \, \frac{1}{2} \, q_z)$, and $\pm\mathbf{Q}_U^{(3)} = \pm(-\frac{1}{2} \, -\frac{1}{2} \, q_z)$, with $q_z \neq 0, \frac{1}{2}$.

Our DFT calculations indeed find that, besides the M_1^+ and L_2^- modes, a phonon mode that transforms as the U_1 irreducible representation and increases the unit cell by $2 \times 2 \times 4$ is also unstable. As presented in Fig. 2, the absolute value of the squared frequency of this U_1 mode is not as large as those of the M_1^+ and L_2^- modes. Whether this implies that the corresponding CDW is a subleading instability as compared to the other two requires further investigation.

While the analysis of the Landau free-energy expansion for the U_i order parameters is beyond the scope of this work, we point out some general properties of these CDW order parameters. Since $\mathbf{Q}_U^{(i)} \neq -\mathbf{Q}_U^{(i)}$, there are 6 wavevectors in the star of U, and as a result, the order parameter $U_{\pm i}$ with $i = 1, 2, 3$ is six-dimensional. Similar terms as those in $\mathcal{F}_L$, Eq. (6), and $\mathcal{F}_{ML}$, Eq. (7), will appear for $\mathcal{F}_U$ and $\mathcal{F}_{UM}$, but with L_iL_j replaced by

$U_i U_{-j}$. Similarly, for the specific case where $q_z = 1/4$, there will also be a trilinear coupling between U_i and L_i of the form $U_i U_j L_k$, with i, j, k all different. The full analysis of this type of U CDW order is a topic for future studies. In the remainder of the paper, we will focus on the commensurate case $q_z = 0$, $1/2$, for which the order parameters are real. Thus, in what follows, we only consider the coupled CDW orders with M and L wave-vectors.

IV. PHASE DIAGRAMS FOR COUPLED CDW ORDERS

Having determined the phase diagrams for the "pure" CDW orders at the M and L points, we now investigate the phase diagram of the coupled case. The difference between $\mathcal{F}_M$ and $\mathcal{F}_L$ is evident from Secs. III A and III B. While the trilinear term present in $\mathcal{F}_M$ ensures that a triple-$\mathbf{Q}_M$ phase is always favored as the leading instability, its absence in $\mathcal{F}_L$ implies that a single-$\mathbf{Q}_L$ phase is favored when $\lambda_L > 0$. Hence, coupling the two terms can be expected to lead to phase diagrams exhibiting a multitude of additional phases.

While the full expression $\mathcal{F}_{\text{tot}}$ is sufficiently complicated that the analytical solutions are no longer tractable, a few insights can be gained before we present the numerical results. Besides the "pure" phases presented in the previous section, our numerical analysis reveals that three different coupled CDW phases, described in Table II and illustrated in Fig. 6, also appear over a wide range of parameters. The superimposed tri-hexagonal Star-of-David CDW state is a triple-$\mathbf{Q}_M$/triple-$\mathbf{Q}_L$ configuration of the form $(MMM) + (LLL)$. We emphasize that, in our notation, for a given i, M_i and L_i have the same sign, whereas $\overline{M}_i$ and L_i have opposite signs. We note that changing the sign of only one set of components, e.g. to $(\overline{MMM}) + (LLL)$, does not change the symmetries of this phase. However, even though they have the same symmetry, these are two distinct phases and, as such, will have different free energies, as evidenced by the γ_M term in the free energy expansion (5) and by the phase diagrams in Fig. 7. We denote these two phases by light and dark blue colors in Table II and in the phase diagrams below. Due to their similarity, hereafter we will simply refer to them both as the superimposed tri-hexagonal Star-of-David phase. The resulting space group of the superimposed tri-hexagonal Star-of-David phases, $P6/mmm$, is the same as the disordered phase and all the "pure" triple-$\mathbf{Q}$ phases: the planar tri-hexagonal phase, the planar Star-of-David phase, and the alternating tri-hexagonal Star-of-David phase discussed in the previous section.

The staggered tri-hexagonal and staggered Star-of-David CDW states are single-$\mathbf{Q}_M$/double-$\mathbf{Q}_L$ phases described by $(M00) + (0LL)$ and $(\overline{M}00) + (0LL)$, respectively. This type of states has been studied previously using DFT in Ref. 33 and proposed to be realized in the
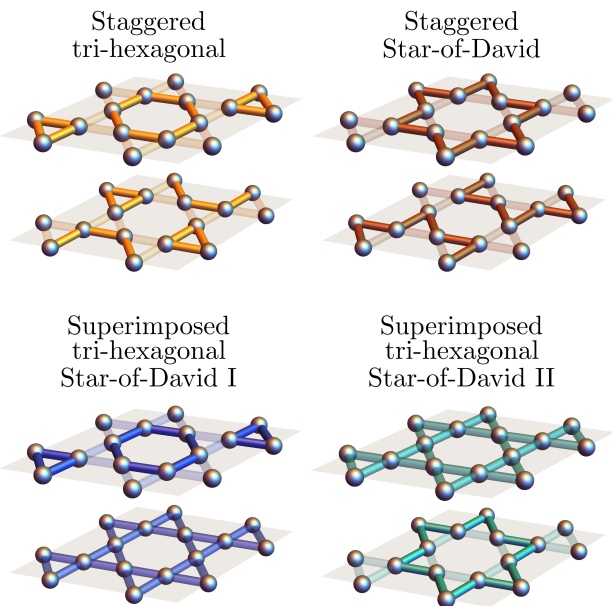

Figure 6. Four possible bond-order patterns arising from the simultaneous condensation of M_i and L_i order parameters, obtained from minimizing the coupled free energy, $\mathcal{F}_{\text{tot}}$. The upper panels show different types of single-$\mathbf{Q}_M$/double-$\mathbf{Q}_L$ order, whereas the lower panels illustrate the triple-$\mathbf{Q}_M$/triple-$\mathbf{Q}_L$ orders. These phases are described by linear combinations of the orders in Figs. 3 and 4, as written in Table II.

kagome metal CsV_3Sb_5. As shown in Fig. 6, they break the sixfold rotational-symmetry of the system, and are described by the space group $Fmmm$. Like the superimposed tri-hexagonal Star-of-David phase, these states increase the unit cell by $2 \times 2 \times 2$. We found that these three coupled CDW configurations can become leading instabilities of the system, which compete with the "pure" CDW orders at M and L over some range of parameters. In contrast, the mixed phases shown in Table III, which were also found in our numerical phase diagrams, only appeared as secondary instabilities inside other phases. They can be interpreted as the superposition of two or more of the phases presented in Tables I and II.

Insight about the emergence of the three coupled CDW states of Table II can be obtained by a qualitative analysis of the different terms of the free-energy $\mathcal{F}_{ML}$ in Eq. (7). The trilinear term, with coefficient γ_{ML}, lowers the total free energy for the triple-$\mathbf{Q}_M$/triple-$\mathbf{Q}_L$ state regardless of the sign of γ_{ML}. It also lowers the free energy of one of the single-$\mathbf{Q}_M$/double-$\mathbf{Q}_L$ phases, but by a smaller amount than for the triple-$\mathbf{Q}_M$/triple-$\mathbf{Q}_L$: either the staggered tri-hexagonal phase, if $\gamma_{ML} < 0$, or the staggered Star-of-David phase, if $\gamma_{ML} > 0$. Notice also that any coupled phase with a single $\mathbf{Q}_L$ component gains no energy from this cubic term – or from any other term of $\mathcal{F}_{\text{tot}}$, for that matter.

The quartic terms of $\mathcal{F}_{ML}$ also impact the three coupled CDW states in distinct ways. For coefficients

Phase	Color	$\mathbf{Q}$-vector	OP	Unit cell	C_6	Space group
Superimposed tri-hexagonal Star-of-David I		$3\mathbf{Q}_M + 3\mathbf{Q}_L$	$(MMM) + (LLL)$	2×2×2	Yes	$P6/mmm$ (#191)
Superimposed tri-hexagonal Star-of-David II		$3\mathbf{Q}_M + 3\mathbf{Q}_L$	$(\overline{MMM}) + (LLL)$	2×2×2	Yes	$P6/mmm$ (#191)
Staggered tri-hexagonal		$\mathbf{Q}_M + 2\mathbf{Q}_L$	$(M00) + (0LL)$	2×2×2	No	$Fmmm$ (#69)
Staggered Star-of-David		$\mathbf{Q}_M + 2\mathbf{Q}_L$	$(\overline{M}00) + (0LL)$	2×2×2	No	$Fmmm$ (#69)

Table II. Summary of the phases that minimize the coupled free energy $\mathcal{F}_{\text{tot}}$ in Eq. (4). All of these phases can occur as leading instabilities of the system. They emerge as a consequence of the coupling terms in $\mathcal{F}_{ML}$ and intertwine the ordered phases with wave-vector $\mathbf{Q}_M$ with those with wave-vector $\mathbf{Q}_L$.

Phase	Color	$\mathbf{Q}$-vector	OP	Unit cell	C_6	Space group
$2M + M + 2L$		$3\mathbf{Q}_M + 2\mathbf{Q}_L$	$(M_1\overline{M}_1 M_2) + (L_1 L_1 0)$	2×2×2	No	$Cccm$ (#66)
$2M + M + 2L + L$		$3\mathbf{Q}_M + 3\mathbf{Q}_L$	$(M_1 M_1 \overline{M}_2) + (L_1 L_1 L_2)$	2×2×2	No	$Cmmm$ (#65)
$M + L + L$		$\mathbf{Q}_M + 2\mathbf{Q}_L$	$(M00) + (0L_1 L_2)$	2×2×2	No	$C2/m$ (#12)

Table III. Additional phases that minimize the coupled free energy $\mathcal{F}_{\text{tot}}$ in Eq. (4). In contrast to the phases in Table II, these states do not occur as leading instabilities of the free energy. They can be described as mixing two or more of the phases in Tables I and II.

$\lambda_{ML}^{(1)}, \lambda_{ML}^{(2)} < 0$, these quartic terms further lower the energy of the triple-$\mathbf{Q}_M$/triple-$\mathbf{Q}_L$ phase, whereas for $\lambda_{ML}^{(1)}, \lambda_{ML}^{(2)} > 0$ they increase its energy. In contrast, the energies of both single-$\mathbf{Q}_M$/double-$\mathbf{Q}_L$ phases are unaffected by these two quartic terms, since they vanish for the configurations $(M00) + (0LL)$ and $(\overline{M}00) + (0LL)$.

This qualitative analysis suggests that coupled CDW states may become energetically more favorable than the pure CDW states in the presence of a large (in magnitude) trilinear coefficient γ_{ML}. The triple-$\mathbf{Q}_M$/triple-$\mathbf{Q}_L$ phase seems generally favored over the single-$\mathbf{Q}_M$/double-$\mathbf{Q}_L$ phases, except when the $\lambda_{ML}^{(1)}$, $\lambda_{ML}^{(2)}$ quartic coefficients are sizable and positive. While this general tendency is confirmed by our numerical calculations, we will see that other terms also play an important role, such as $\lambda_{ML}^{(3)}$ and the coefficients γ_M and λ_L of the "pure" free energies. For instance, γ_{ML} and γ_M may be incompatible if they have opposite signs; for example, $\gamma_M < 0$ favors (MMM) whereas $\gamma_{ML} > 0$ favors $(\overline{MMM})$. Similarly, λ_L favors either a single-$\mathbf{Q}_L$ or a triple-$\mathbf{Q}_L$ phase, but not a double-$\mathbf{Q}_L$ phase, which does not even appear in the phase diagram of the L_i CDW states.

We finish by noting that, due to the sizable parameter space, we cannot rule out that other coupled CDW states may be stabilized outside the regimes we investigated. For instance, there are several possible mixed phases that can emerge inside the ordered states discussed above. A few of these mixed phases were seen in our numerical calculations (see Table III), all of which break sixfold rotational symmetry.

A. Impact of the coupling between M_i and L_i

Here, we illustrate how the coupling between $\mathcal{F}_M$ and $\mathcal{F}_L$ modifies the "pure" phase diagrams in Fig.

γ_M	λ_M	u_M	λ_L	u_L	γ_{ML}	$\lambda_{ML}^{(1)}$	$\lambda_{ML}^{(2)}$	$\lambda_{ML}^{(3)}$
						0.01	0.015	0.0175
0.25	0.6	1.2	0.8	1.5	-0.7	0.5	0.75	0.875
						1.0	1.5	1.75

Table IV. Parameters used for the numerical minimization presented in Sec. IV (unless the specific parameter is being varied as indicated in the text). The three rows of $\lambda_{ML}^{(i)}$ denote the three different sets used in Fig. 7. In Figs. 8–10 we use the middle row values for $\lambda_{ML}^{(i)}$.

5. In Fig. 7 we show the numerically-calculated γ_{ML}-temperature phase diagrams for $T_L > T_M$ [panels (a)–(c)] and $T_M > T_L$ [panels (d)–(f)]. The phases are labeled according to the color scheme of Tables I, II, and III. The dashed (dotted) line denotes T_L (T_M) in this and all subsequent figures. Upon moving from the top to the bottom panels, progressively larger values of the quartic couplings $\lambda_{ML}^{(i)}$ are considered, as shown in the last three columns of Table IV. The coefficients of the uncoupled free energies are set by the values in the first five columns of the same table. Because we consider positive values for the "pure" coefficients γ_M, λ_M, and λ_L, the leading instabilities in the uncoupled cases are an alternating stripe phase (L_i case) and a planar Star-of-David phase (M_i case). The addition of finite $\lambda_{ML}^{(i)}$ and γ_{ML} changes this, and several additional phases appear.

Starting with the case $T_L > T_M$ [panels (a)–(c)] in Fig. 7, for small values of γ_{ML} the leading instability remains the alternating stripe phase (green). It gives way to one of the superimposed tri-hexagonal Star-of-David phases (light/dark blue) as the magnitude of γ_{ML} increases. The staggered tri-hexagonal phase (orange) appears as a sub-leading instability in the $\gamma_{ML} < 0$ region, condensing at a lower temperature inside the superimposed tri-hexagonal Star-of-David phase. Other mixed phases presented in Table III appear for narrow ranges of
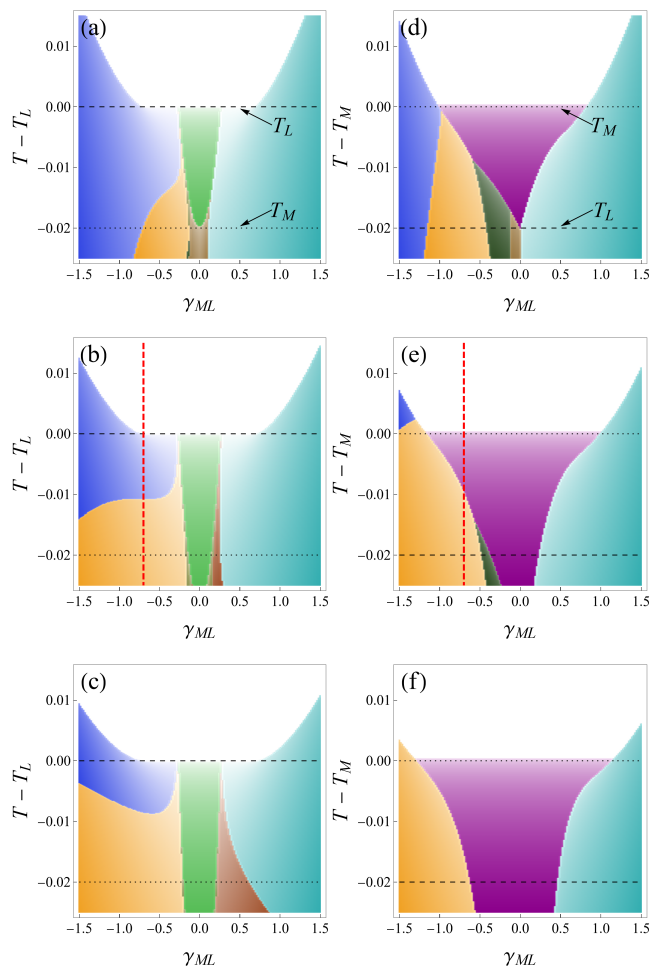
Figure 7. Phase diagrams for coupled M and L CDW orders for progressively larger values of $\lambda_{ML}^{(i)}$ (top to bottom) as functions of γ_{ML} and T. The parameters used are summarized in Table IV. The dashed black line denotes T_L and the dotted black line denotes T_M. The color scheme is that summarized in Tables I, II, and III. For panels (a)-(c), $T_L > T_M$ and in (d)-(f), $T_M > T_L$. The value of γ_{ML} required to change the leading instability from a "pure" CDW phase to a coupled CDW phase is much smaller for $T_L > T_M$ compared to $T_M > T_L$. While the alternating stripe phase (green) appearing for $T_L > T_M$ is rather unaffected by an increasing $\lambda_{ML}^{(i)}$, the planar Star-of-David phase (dark purple) appearing for $T_M > T_L$ becomes more prominent as $\lambda_{ML}^{(i)}$ increases. The red dashed line denotes the value of γ_{ML} chosen in Figs. 8–10.

γ_{ML} at low temperatures. Upon increasing the positive-valued coefficients $\lambda_{ML}^{(i)}$ (i.e. moving from (a) to (c)), the staggered tri-hexagonal phase becomes more prominent. At the same time, the staggered Star-of-David phase (brown) emerges in the $\gamma_{ML} > 0$ region of the phase diagram, although it occupies a smaller area than its counterpart in the $\gamma_{ML} < 0$ region. The staggered tri-hexagonal and star-of-David phases do not become the leading instabilities for the parameters studied in panels (a)–(c).

Moving on to the case $T_M > T_L$ [panels (d)–(f) in Fig. 7], the planar Star-of-David phase (dark purple) remains the leading instability for a large range of γ_{ML} values – larger than the range for which the alternating stripe phase appears in panels (a)–(c). This range of γ_{ML} values is only weakly dependent on the magnitude of $\lambda_{ML}^{(i)}$, as one moves from panel (d) to panel (f). Larger absolute values of γ_{ML} in panel (d) change the leading CDW instability to one of the superimposed tri-hexagonal Star-of-David phases (light/dark blue), although the staggered tri-hexagonal phase (orange) emerges at lower temperatures. Increasing $\lambda_{ML}^{(i)}$ as one moves from (d) to (f), the staggered tri-hexagonal phase expands and becomes the dominant and only leading instability for γ_{ML} negative and large in magnitude. For large enough $\gamma_{ML} > 0$, the superimposed tri-hexagonal Star-of-David phase remains the leading instability for all values of $\lambda_{ML}^{(i)}$ studied here. In contrast to the case $T_L > T_M$ [panels (a)–(c)], the staggered Star-of-David phase does not appear on the $\gamma_{ML} > 0$ side of the phase diagrams (d)–(f). One possible explanation is that, because $\gamma_M > 0$ (see Table IV), when $\gamma_{ML} > 0$ the superimposed tri-hexagonal Star-of-David II phase (light blue) becomes more robust as compared to the case when $\gamma_{ML} < 0$, since the two cubic terms favor the same $\text{sign}(M_1 M_2 M_3)$ only when the two coefficients have the same sign.

B. Robustness of the phase diagrams

The behavior of the phase diagrams shown in Fig. 7 generally agrees with our qualitative analysis: a coupled CDW phase is stabilized and wins over the "pure" CDW phase (green or purple) when the trilinear coefficient γ_{ML} is relatively large (in magnitude). For most of the phase diagram, the dominant coupled CDW state is one of the superimposed tri-hexagonal Star-of-David phases (light/dark blue), although upon increasing the values of the positive quartic coefficients $\lambda_{ML}^{(i)}$, the staggered tri-hexagonal phase (orange) becomes more prominent in the $\gamma_{ML} < 0$ side of the phase diagram.

We now consider the impact of further varying the various parameters of $\mathcal{F}_{\text{tot}}$ to elucidate the robustness of the phase diagrams of Fig. 7. In particular, we are interested in establishing under which conditions the leading instability is towards one of the coupled CDW phases that break sixfold rotational symmetry – i.e. the staggered tri-hexagonal (orange) and staggered Star-of-David (brown) phases.

We focus on the set of parameters given by the central row of Table IV, marked by the vertical red dashed lines in Figs. 7(b) and 7(e). In particular, across Figs. 8–10, we fix $\gamma_{ML} = -0.7$ and vary the other eight parameters that appear, respectively, in $\mathcal{F}_M$, $\mathcal{F}_L$, and $\mathcal{F}_{ML}$, for both $T_L > T_M$ (left panels) and $T_M > T_L$ (right panels). In these figures, the arrows denote the parameter values corresponding to the red dashed lines of Figs. 7(b) and
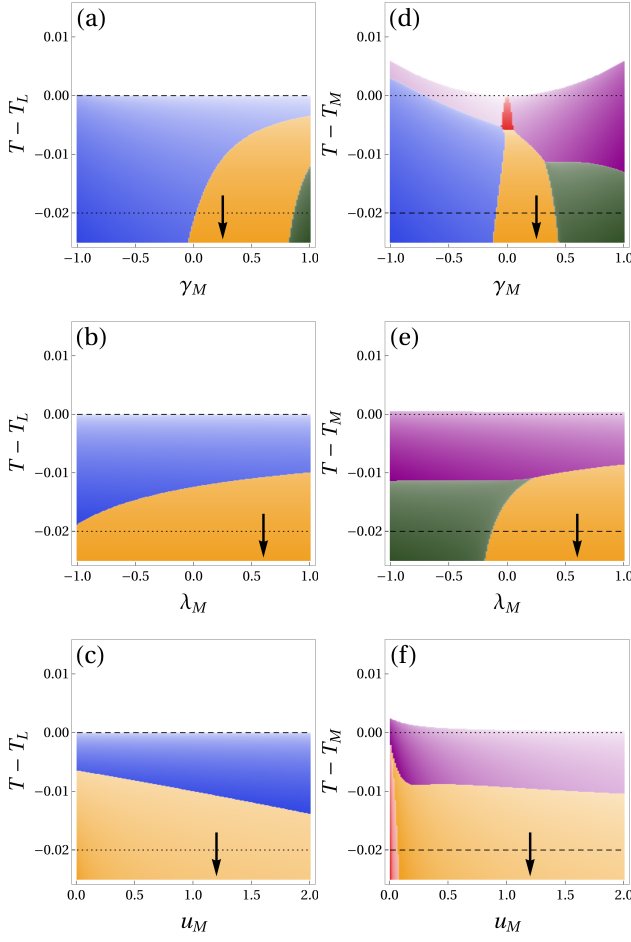
Figure 8. Impact of changing the coefficients γ_M, λ_M, and u_M of $\mathcal{F}_M$, for fixed $\gamma_{ML} = -0.7$, on the phase diagrams of Figs. 7(b) and 7(e). Panels (a)–(c) correspond to $T_L > T_M$ and (d)–(f), to $T_M > T_L$. The arrows denote the parameters' values corresponding to the dashed lines in Figs. 7(b) and 7(e). For the majority of cases, the leading instabilities are unaffected by changing these parameters. The only exception is the case of γ_M which, for $T_M > T_L$ [panel (d)], causes a change from the planar tri-hexagonal to the planar Star-of-David phase. In this regime, the behavior is reminiscent of that observed in the "pure" phase diagram Fig. 5(a), indicating that L_i plays nearly no role in this region of the phase diagram. In addition, changing γ_M leads to a variety of additional phases at lower temperatures. In general, the impact of changing the parameters of $\mathcal{F}_M$ is the greatest when $T_M > T_L$, and the M_i are the leading order parameters [panels (d)–(f)].

Figure 9. Impact of changing the coefficients λ_L and u_L of $\mathcal{F}_L$, for fixed $\gamma_{ML} = -0.7$, on the phase diagrams of Figs. 7(b) and 7(e). Panels (a)–(b) correspond to $T_L > T_M$ and (c)–(d), to $T_M > T_L$. The arrows denote the parameters values corresponding to the dashed lines in Figs. 7(b) and 7(e) while the red dotted line denotes the value of u_L chosen in Fig. 11(a)–(d). Overall, the impact of changing these parameters is minor, except for small values of u_L, where the leading instability becomes the staggered tri-hexagonal phase (orange) rather than the superimposed tri-hexagonal Star-of-David I phase (dark blue).

7(e), which are the same as those presented in the central row of Table IV.

We start by analyzing the impact of the changes in the coefficients of $\mathcal{F}_M$ in Fig. 8. From simple power counting, the cubic coefficient γ_M is expected to have a stronger impact on the phase diagram compared to the quartic coefficients λ_M and u_M. This expectation is confirmed by the plots in Fig. 8. Although changing γ_M leads to the appearance of a variety of additional phases as secondary
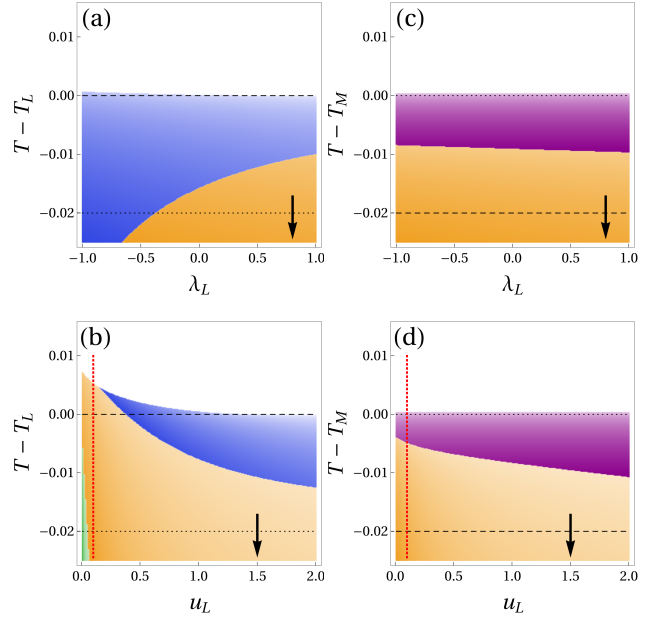
transitions, it does not alter the leading instabilities, except for the finely tuned case at $\gamma_M = 0$. Therefore, γ_{ML} remains the most important of the two cubic coefficients to determine the leading instability. Note that the superimposed tri-hexagonal Star-of-David phases (light/dark blue) become more robust when the signs of γ_M and γ_{ML} are the same, in agreement with what we discussed above.

The coefficients λ_M and u_M, on the other hand, have a more limited effect, although λ_M does lead to a few changes at lower temperatures when the M_i order parameters are dominant, i.e. $T_M > T_L$ [Figs. 8(d)–8(f)]. Note that u_M must be positive for the free energy to remain bounded, as argued in Sec. III A. In Figs. 8(d) and 8(e), we observe the appearance of a state that mixes a triple-$\mathbf{Q}_M$ phase with a double-$\mathbf{Q}_L$ phase (dark green), described by three distinct order parameters, $(M_1\overline{M}_1 M_2) + (L_1 L_1 0)$, as shown in Table III.

Moving on to Fig. 9, we consider the impact of the two coefficients of $\mathcal{F}_L$. While changing λ_L does not lead to a qualitatively different phase diagram, it has a minor impact on the onset temperature of the secondary transition in the case $T_L > T_M$, as seen in panel (a). On the other hand, u_L prominently impacts the phase diagrams, inducing a transition between the staggered tri-hexagonal phase (orange) and the superimposed tri-hexagonal Star-
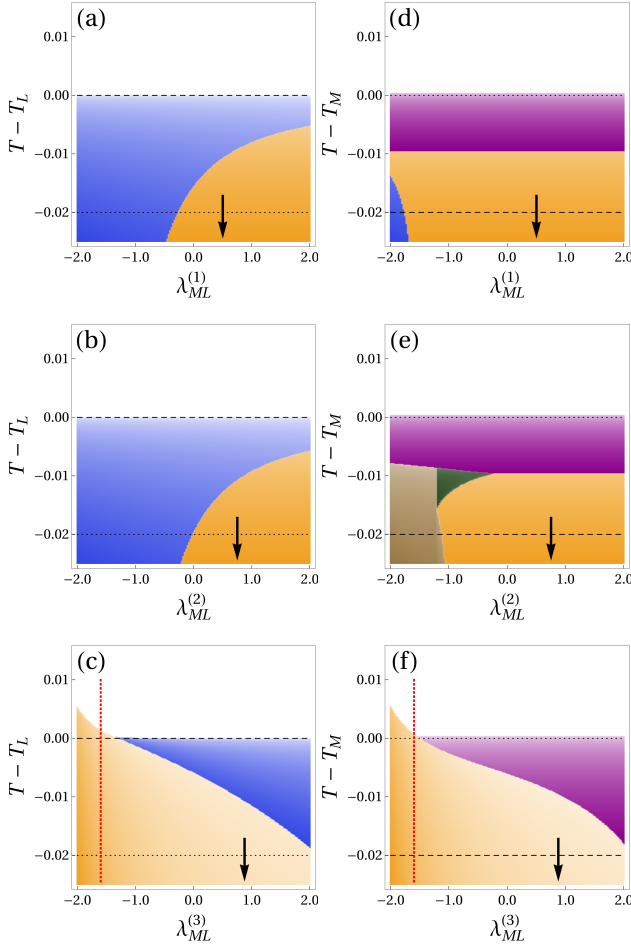
Figure 10. Impact of changing the coefficients $\lambda_{ML}^{(1)}$, $\lambda_{ML}^{(2)}$, and $\lambda_{ML}^{(3)}$ of $\mathcal{F}_{ML}$, for fixed $\gamma_{ML} = -0.7$, on the phase diagrams of Figs. 7(b) and (e). Panels (a)–(c) correspond to $T_L > T_M$ and (d)–(f), to $T_M > T_L$. The arrows denote the parameters values corresponding to the dashed lines in Figs. 7(b) and (e) while the red dotted line denotes the value of $\lambda_{ML}^{(3)}$ chosen in Fig. 11(e)–(h). The coefficients $\lambda_{ML}^{(1)}$ and $\lambda_{ML}^{(2)}$ do not change the leading instabilities, affecting only the secondary transitions at lower temperatures. On the other hand, when $\lambda_{ML}^{(3)}$ is negative, it can change the leading transition to the staggered tri-hexagonal phase (orange), regardless of whether $T_L > T_M$ [panel (c)] or $T_M > T_L$ [panel (f)].

of-David I phase (dark blue) as the leading instability of the system. Such a transition occurs for a very small value of u_L. Although the transition is only seen for $T_L > T_M$ [panel (b)], a similar trend is seen in the case $T_M > T_L$ [panel (d)].

Figure 10 shows the effect of the coupling constants $\lambda_{ML}^{(i)}$. Generally, their main impact is on the shape of the phase diagrams below the leading transition temperature. The only exception is the case of $\lambda_{ML}^{(3)}$: negative values of this coefficient stabilize the staggered tri-hexagonal phase (orange) as the leading instability of the system. We emphasize that the free energy remains bounded in

all cases studied here.

Overall, the analyses presented in Figs. 8–10 reveal that, at least in what concerns the leading instabilities, the phase diagrams of Fig. 7 are rather robust against independent variations of the other eight Landau coefficients. This confirms that it is the cubic coefficient γ_{ML} of $\mathcal{F}_{ML}$ which is responsible for promoting a coupled M-L CDW state, with the quartic coefficients $\lambda_{ML}^{(i)}$ and the relative sign of γ_M with respect to γ_{ML} selecting between the triple-$\mathbf{Q}_M$/triple-$\mathbf{Q}_L$ phase and the single-$\mathbf{Q}_M$/double-$\mathbf{Q}_L$ phase. We emphasize once again that the nine-dimensional parameter space is vast, and thus we cannot rule out the appearance of other states.

C. Sixfold-rotational symmetry breaking phases

Recent experiments on kagome metals are consistent with a CDW state that doubles the unit cell in all directions ($2 \times 2 \times 2$ unit cell) and lowers the sixfold-rotational symmetry of the lattice to twofold [23, 24, 26, 31, 33]. In this subsection, we further explore the possibility of obtaining such a CDW phase as the leading instability of the system. The breaking of the sixfold rotational symmetry is signaled by the onset of three nematic order parameters:

$$\Phi_M = \begin{pmatrix} M_1^2 + M_3^2 - 2M_2^2 \\ \sqrt{3}\left(M_3^2 - M_1^2\right) \end{pmatrix}, \tag{18}$$

$$\Phi_L = \begin{pmatrix} L_1^2 + L_3^2 - 2L_2^2 \\ \sqrt{3}\left(L_3^2 - L_1^2\right) \end{pmatrix}, \tag{19}$$

$$\Phi_{ML} = \begin{pmatrix} M_1 L_2 L_3 + M_3 L_1 L_2 - 2M_2 L_1 L_3 \\ \sqrt{3}\left(M_3 L_1 L_2 - M_1 L_2 L_3\right) \end{pmatrix}. \tag{20}$$

Each of them, obtained using the INVARIANTS tool [47], transforms as the Γ_5^+ irreducible representation of the space group $P6/mmm$. Γ_5^+ is the irreducible representation corresponding to three-state Potts-nematic order [53, 54] in a lattice with sixfold or threefold rotational symmetry, and it is subducted to the E_{2g} irreducible representation of the D_{6h} point group [55].

The above composite order parameters are useful to determine whether a specific CDW phase breaks the sixfold rotational symmetry. Referring to Table I, as one might have expected, the stripe single-$\mathbf{Q}_M$ and single-$\mathbf{Q}_L$ phases lead to finite Φ_M and Φ_L, respectively; however, the unit cell does not double in all three directions. On the other hand, the "pure" triple-$\mathbf{Q}_M$ and triple-$\mathbf{Q}_L$ phases – planar tri-hexagonal, planar Star-of-David, and superimposed tri-hexagonal Star-of-David – do not result in a finite Φ_M or Φ_L, and thus do not break the six-fold rotational symmetry of the system.

Meanwhile, the coupling between M_i and L_i allows for coupled CDW phases that do break the six-fold rotational symmetry and double the unit cell in all directions, being consistent with experimental observations [23, 27, 28]. Referring to Table II, Φ_M, Φ_L, and Φ_{ML} are all nonzero
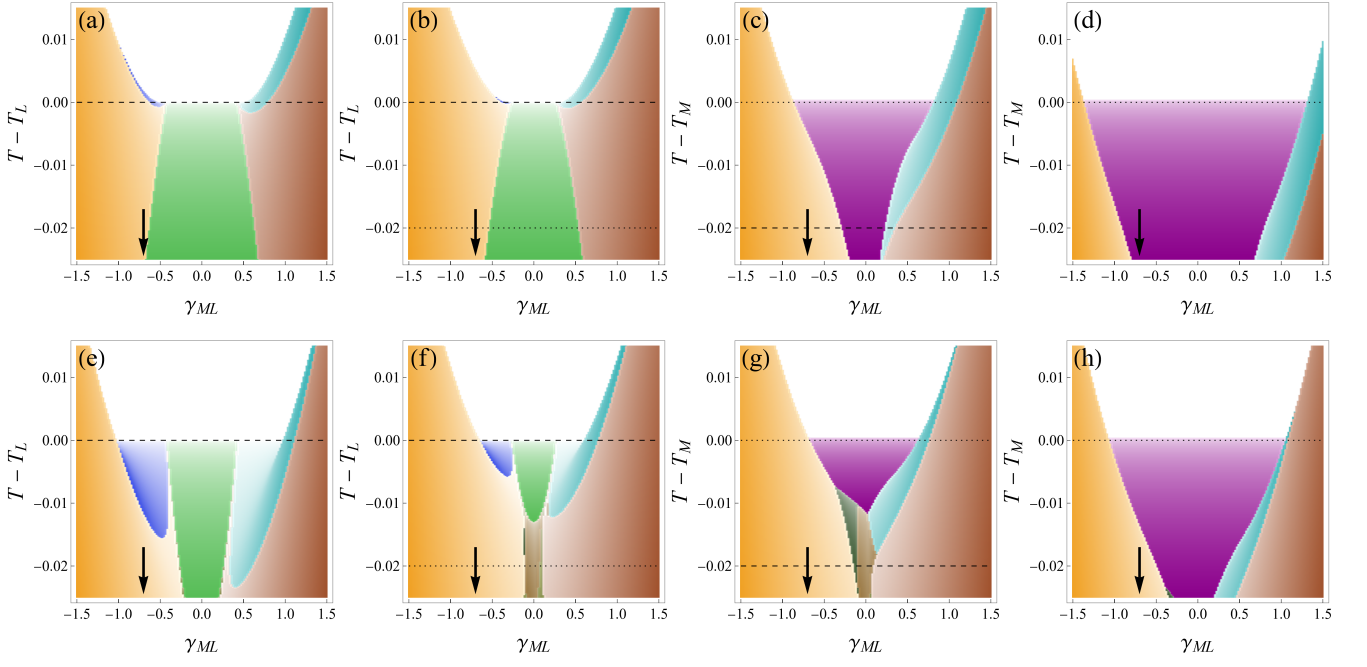
Figure 11. Phase diagrams for $u_L = 0.1$ (a)–(d) [see red dotted line in Fig. 9(b) and (d)] and $\lambda_{ML}^{(3)} = -1.6$ (e)–(h) [see red dotted line in Figs. 10(c) and (f)] for different values of $T_L - T_M$, from $T_L - T_M = -0.05$ (a), (e) to $T_L - T_M = 0.05$ (d), (h). T_M and T_L are denoted by the dotted and dashed black lines respectively. The remaining parameters are as presented in Table IV.

for the two types of single-$\mathbf{Q}_M$/double-$\mathbf{Q}_L$ phases, described by $(M00) + (0LL)$ (staggered tri-hexagonal) and $(\overline{M}00) + (0LL)$ (staggered star-of-David). On the other hand, the triple-$\mathbf{Q}_M$/triple-$\mathbf{Q}_L$ superimposed tri-hexagonal Star-of-David phase, given by $(MMM) + (LLL)$, preserves the sixfold rotational symmetry.

There are other potential coupled CDW phases that also break C_6 symmetry, but either we do not find them, or they emerge only as subleading instabilities inside another ordered state. Consider, for instance, the double-$\mathbf{Q}_M$/single-$\mathbf{Q}_L$ phase with $(MM0) + (00L)$ discussed in Ref. 33; it has $\Phi_M, \Phi_L \neq 0$ but $\Phi_{ML} = 0$. The reason we believe it does not show up in the phase diagrams is because it does not gain any energy from the trilinear term of $\mathcal{F}_{ML}$. Conversely, the triple-$\mathbf{Q}_M$/triple-$\mathbf{Q}_L$ phases described by $(MM\overline{M}) + (LLL)$ and $(MMM) + (LL\overline{L})$ have $\Phi_M, \Phi_L = 0$ but $\Phi_{ML} \neq 0$. While it gains energy from the cubic and quartic terms of $\mathcal{F}_{ML}$, it seems to be not able to compete with the other phases seen in our phase diagrams. This analysis also indicates that neither of these phases are likely to be leading instabilities of the system. The reason is because only a subset of the composite nematic order parameters Φ_i are nonzero. Symmetry imposes that, once one of the Φ_i is non-zero, all the other ones will become nonzero as well, since they all belong to the same irreducible representation Γ_5^+. But, clearly, the only way this can happen for, say, the $(MM\overline{M}) + (LLL)$ phase, is by further making at least one of the three M_i or L_i components different from the others. This indicates that this phase is

actually one of the mixed states shown in Table III, i.e. the $(MM\overline{M}) + (LLL)$ phase necessarily mixes with other phase(s) to become $(M_1 M_1 \overline{M}_2) + (L_1 L_1 L_2)$.

Therefore, we conclude that the most promising candidates to explain the experimental observation of C_6 symmetry-breaking and $2 \times 2 \times 2$ unit cell enhancement are the staggered tri-hexagonal phase (orange) and staggered Star-of-David phase (brown) depicted in Fig. 6. The main question is whether they appear as a secondary instability inside the superimposed tri-hexagonal Star-of-David phases (light/dark blue) or as the leading instability of the system. Based on the results from Figs. 7–10, besides large and positive $\lambda_{ML}^{(1)}$ and $\lambda_{ML}^{(2)}$, two coefficients stand out as promoting the onset of the staggered tri-hexagonal phase as the leading instability: u_L [see red dotted lines in Figs. 9(b) and 9(d)] and $\lambda_{ML}^{(3)}$ [see red dotted lines in Figs. 10(c) and 10(f)]. To further elucidate whether the parameter range where this state is the leading instability of the system can be enhanced, in Fig. 11 we show γ_{ML}-temperature phase diagrams starting with parameters corresponding to the red dotted lines of Figs. 9(b) and 9(d) [arrows in panels (a)–(d)] and the red dotted lines of Figs. 10(c) and 10(f) [arrows in panels (e)–(h)]. In particular, we interpolate between the L-dominated case (left most panels, $T_L \gg T_M$) and the M-dominated case (right most panels, $T_M \gg T_L$). While these parameter choices are obviously not exhaustive, they do represent the cases that we found to be the most favorable for the staggered tri-hexagonal phase.

From Fig. 11, it is clear that the staggered tri-

hexagonal phase (orange) only occurs as a leading instability for large (in magnitude) negative values of γ_{ML}. For smaller (in magnitude) negative values, it can appear only as a secondary transition inside another phase. The center of the phase diagrams remain dominated by the "pure" alternating stripe (green) and the planar Star-of-David (dark purple) phases. Interestingly, there is an asymmetry in the phase diagram since even for large positive γ_{ML}, the staggered Star-of-David phase (brown) does not become the leading instability of the system. This is a consequence of the fact that we chose $\gamma_M > 0$. Had we considered $\gamma_M < 0$ instead, the superimposed tri-hexagonal Star-of-David II phase (light blue) envelope appearing above the staggered Star-of-David phase (brown) would appear above the staggered tri-hexagonal phase (orange) instead, and would be a superimposed tri-hexagonal Star-of-David I (dark blue) phase instead. As a result, the staggered Star-of-David phase would become the leading instability for sufficiently large positive γ_{ML}.

It is interesting to note how the difference in the bare transition temperatures, T_L and T_M, affects the shape of the phase diagrams. As they correspond to the condensation of order parameters belonging to different irreducible representations, they are not guaranteed to be close. In both cases ($T_L > T_M$ and $T_M > T_L$), upon moving to the left of the phase diagram along the negative γ_{ML} axis, the staggered tri-hexagonal phase (orange) first emerges as a secondary instability before becoming the leading instability. However, when $T_L > T_M$ [panels (a)–(b) and (e)–(f)], it is generally preceded by either of the superimposed tri-hexagonal Star-of-David phases (light/dark blue), whereas when $T_M > T_L$ [panels (c)–(d) and (g)–(h)], it is achieved via a direct transition from the "pure" Star-of-David phase (dark purple). More generally, it is clear that for both M and L to condense simultaneously, the cubic coefficient γ_{ML} must overcome the splitting between T_L and T_M. Whether this is facilitated in AV$_3$Sb$_5$ by an intrinsically large trilinear coefficient or by an accidental near-degeneracy of T_L and T_M requires a microscopic model and is beyond the scope of this work.

We finish this section by noting that it is possible for CDW fluctuations to lead to the condensation of the composite nematic order parameters in Eqs. (18) even when $M_i = L_i = 0$, i.e. above the CDW transition [56]. Such a vestigial nematic phase arising from partially-melted CDW order has been recently proposed in the case of tetragonal Ni-based pnictide superconductors [57]. To the best of our knowledge, no evidence of a separate nematic transition has been reported in AV$_3$Sb$_5$.

V. SUMMARY AND CONCLUSIONS

In this paper, we derived the Landau free energy appropriate for studying coupled CDWs with wave-vectors at both the M and L points of the hexagonal BZ. In the absence of coupling between the M_i and L_i order parameters, the phase diagrams feature very little variation. For the M-point CDW, due to the presence of a trilinear term, only a triple-$\mathbf{Q}_M$ phase, corresponding to either the planar tri-hexagonal or planar Star-of-David bond configuration, occurs as a leading instability. Because a cubic term is not allowed for the L-point CDW, the phase diagram features both a single-$\mathbf{Q}_L$ (alternating stripe) and a triple-$\mathbf{Q}_L$ (alternating tri-hexagonal Star-of-David) phase. This simple picture changes dramatically once the M- and L-point CDWs are coupled. Crucially, owing to the specific wave-vectors of the order parameters at M and L, both cubic and quartic coupling terms are allowed. The trilinear coupling, γ_{ML}, plays a primary role in determining the leading instability as evidenced from Figs. 7–11.

Importantly, even if the transition temperatures T_L and T_M of the pure CDW states are not extremely close, a large enough (in magnitude) trilinear coupling γ_{ML} is able to stabilize a coupled M-L CDW state. In this case, while for most of the parameter space studied here the leading coupled instability is the triple-$\mathbf{Q}_M$/triple-$\mathbf{Q}_L$ state dubbed superimposed tri-hexagonal Star-of-David phase, we also find a range of parameters for which the leading instability is the single-$\mathbf{Q}_M$/double-$\mathbf{Q}_L$ states dubbed staggered tri-hexagonal and staggered Star-of-David phases. These phases are interesting because they not only double the size of the unit cell in all directions, but they also break the sixfold rotational symmetry of the lattice via the condensation of secondary composite nematic order parameters. These two features are consistent with several experimental observations regarding the CDW state of AV$_3$Sb$_5$ kagome metals [23, 24, 26, 31].

This phenomenological analysis raises interesting questions that deserve further experimental investigation. For instance, a direct transition to one of the single-$\mathbf{Q}_M$/double-$\mathbf{Q}_L$ states seems to require specially tuned Landau parameters. Most commonly, this state onsets inside either the triple-$\mathbf{Q}_M$/triple-$\mathbf{Q}_L$ state or one of the "pure" triple-$\mathbf{Q}_M$ states (i.e. the planar tri-hexagonal and planar Star-of-David phases). Therefore, it is crucial to experimentally establish whether there is a single or multiple CDW transitions in AV$_3$Sb$_5$. This will provide important constraints on the Landau parameters. Similarly, it will be important to determine whether the breaking of sixfold rotational symmetry takes place above, simultaneously with, or below the first CDW transition. Which of these scenarios is realized depends roughly on the size of the trilinear coupling γ_{ML} relative to the energy difference between the pure M-point and pure L-point CDW states. Given the sensitivity of the phase diagram to these two parameters, it is conceivable that AV$_3$Sb$_5$ compounds with different alkali metals A may show distinct CDW phase diagrams.

Our results also provide insights about the microscopic mechanism responsible for the onset of CDW order. Our DFT calculations reveal two interesting features associated with the CDW state: (i) three different phonon modes along the U line (which includes the

M and L points) are unstable; and (ii) the corresponding imaginary-valued frequencies display a strong dependence on the electronic temperature (as signaled by the Fermi surface smearing). Taken together, they provide strong support for the scenario in which the CDW is not the consequence of a pure lattice instability, but is driven by the electronic degrees of freedom. More specifically, because all points along the U line share the same in-plane momentum, this suggests a primary role of the in-plane electronic dispersion and/or interactions in promoting the CDW transition. Importantly, an electronically-driven CDW instability is likely to have a more significant intertwining with the superconducting state. This is supported by recent transport measurements indicating a strong competition between the CDW

and SC phases [30].

[1] L. Balents. *Spin liquids in frustrated magnets.* Nature **464**, 199 (2010).

[2] Mingu Kang, Linda Ye, Shiang Fang, Jhih-Shih You, Abe Levitan, Minyong Han, Jorge I. Facio, Chris Jozwiak, Aaron Bostwick, Eli Rotenberg, Mun K. Chan, Ross D. McDonald, David Graf, Konstantine Kaznatcheev, Elio Vescovo, David C. Bell, Efthimios Kaxiras, Jeroen van den Brink, Manuel Richter, Madhav Prasad Ghimire, Joseph G. Checkelsky, and Riccardo Comin. *Dirac fermions and flat bands in the ideal kagome metal FeSn.* Nat. Mater. **19**, 163 (2019).

[3] Mingu Kang, Shiang Fang, Linda Ye, Hoi Chun Po, Jonathan Denlinger, Chris Jozwiak, Aaron Bostwick, Eli Rotenberg, Efthimios Kaxiras, Joseph G. Checkelsky, and Riccardo Comin. *Topological flat bands in frustrated kagome lattice CoSn.* Nat. Commun. **11**, 4004 (2020).

[4] William R. Meier, Mao-Hua Du, Satoshi Okamoto, Narayan Mohanta, Andrew F. May, Michael A. McGuire, Craig A. Bridges, German D. Samolyuk, and Brian C. Sales. *Flat bands in the CoSn-type compounds.* Phys. Rev. B **102**, 075148 (2020).

[5] H.-M. Guo and M. Franz. *Topological insulator on the kagome lattice.* Phys. Rev. B **80**, 113102 (2009).

[6] I. I. Mazin, Harald O. Jeschke, Frank Lechermann, Hunpyo Lee, Mario Fink, Ronny Thomale, and Roser Valentí. *Theoretical prediction of a strongly correlated Dirac metal.* Nat. Commun. **5**, 4261 (2014).

[7] R. Nandkishore, L. S. Levitov, and A. V. Chubukov. *Chiral superconductivity from repulsive interactions in doped graphene.* Nat. Phys. **8**, 158 (2012).

[8] Maximilian L. Kiesel and Ronny Thomale. *Sublattice interference in the kagome Hubbard model.* Phys. Rev. B **86**, 121105(R) (2012).

[9] Maximilian L. Kiesel, Christian Platt, and Ronny Thomale. *Unconventional Fermi Surface Instabilities in the Kagome Hubbard Model.* Phys. Rev. Lett. **110**, 126405 (2013).

[10] Rahul Nandkishore, Ronny Thomale, and Andrey V. Chubukov. *Superconductivity from weak repulsion in hexagonal lattice systems.* Phys. Rev. B **89**, 144501 (2014).

[11] Brenden R. Ortiz, Lídia C. Gomes, Jennifer R. Morey, Michal Winiarski, Mitchell Bordelon, John S. Mangum, Iain W. H. Oswald, Jose A. Rodriguez-Rivera, James R. Neilson, Stephen D. Wilson, Elif Ertekin, Tyrel M. McQueen, and Eric S. Toberer. *New kagome prototype materials: discovery of KV_3Sb_5, RbV_3Sb_5, and CsV_3Sb_5.* Phys. Rev. Mat. **3**, 094407 (2019).

[12] Brenden R. Ortiz, Samuel M. L. Teicher, Yong Hu, Julia L. Zuo, Paul M. Sarte, Emily C. Schueller, A. M. Milinda Abeykoon, Matthew J. Krogstad, Stephan Rosenkranz, Raymond Osborn, Ram Seshadri, Leon Balents, Junfeng He, and Stephen D. Wilson. *CsV_3Sb_5: A $\mathbb{Z}_2$ Topological Kagome Metal with a Superconducting Ground State.* Phys. Rev. Lett. **125**, 247002 (2020).

[13] Brenden R. Ortiz, Paul M. Sarte, Eric M. Kenney, Michael J. Graf, Samuel M. L. Teicher, Ram Seshadri, and Stephen D. Wilson. *Superconductivity in the Z2 kagome metal KV_3Sb_5.* Phys. Rev. Mat. **5**, 034801 (2021).

[14] Qiangwei Yin, Zhijun Tu, Chunsheng Gong, Yang Fu, Shaohua Yan, and Hechang Lei. *Superconductivity and normal-state properties of kagome metal RbV_3Sb_5 single crystals.* Chin. Phys. Lett. **38**, 037403 (2021).

[15] Yanpeng Song, Tianping Ying, Xu Chen, Xu Han, Yuan Huang, Xianxin Wu, Andreas P. Schnyder, Jian-Gang Guo, and Xiaolong Chen. *Competition of superconductivity and charge density wave in selective oxidized CsV3Sb5 thin flakes.* arXiv:2105.09898 (2021).

[16] Feng Du, Shuaishuai Luo, Brenden R. Ortiz, Ye Chen, Weiyin Duan, Dongting Zhang, Xin Lu, Stephen D. Wilson, Yu Song, and Huiqiu Yuan. *Pressure-induced double superconducting domes and charge instability in the kagome metal KV_3Sb_5.* Phys. Rev. B **103**, L220504 (2021).

[17] C. C. Zhao, L. S. Wang, W. Xia, Q. W. Yin, J. M. Ni, Y. Y. Huang, C. P. Tu, Z. C. Tao, Z. J. Tu, C. S. Gong, H. C. Lei, Y. F. Guo, X. F. Yang, and S. Y. Li. *Nodal superconductivity and superconducting domes in the topological Kagome metal CsV_3Sb_5.* arXiv:2102.08356 (2021).

[18] Zhuyi Zhang, Zheng Chen, Ying Zhou, Yifang Yuan, Shuyang Wang, Jing Wang, Haiyang Yang, Chao An, Lili Zhang, Xiangde Zhu, Yonghui Zhou, Xuliang Chen, Jianhui Zhou, and Zhaorong Yang. *Pressure-induced reemergence of superconductivity in the topological kagome metal CsV_3Sb_5.* Phys. Rev. B **103**, 224513 (2021).

[19] K.-Y. Chen, N.-N. Wang, Q.-W. Yin, Y.-H. Gu, K. Jiang,

Z.-J. Tu, C.-S. Gong, Y. Uwatoko, J.-P. Sun, H.-C. Lei, J.-P. Hu, and J.-G. Cheng *Double superconducting dome and triple enhancement of Tc in the kagome superconductor CsV_3Sb_5 under high pressure.* Phys. Rev. Lett. **126**, 247001 (2021).

[20] C. C. Zhu, X. F. Yang, W. Xia, Q. W. Yin, L. S. Wang, C. C. Zhao, D. Z. Dai, C. P. Tu, B. Q. Song, Z. C. Tao, Z. J. Tu, C. S. Gong, H. C. Lei, Y. F. Guo, S. Y. Li. *Double-dome superconductivity under pressure in the V-based Kagome metals AV3Sb5 (A = Rb and K).* arXiv:2104.14487 (2021).

[21] E. Uykur, B. R. Ortiz, S. D. Wilson, M. Dressel, A. A. Tsirlin. *Optical detection of charge-density-wave instability in the non-magnetic kagome metal KV3Sb5.* arXiv:2103.07912 (2021).

[22] Xiaoxiang Zhou, Yongkai Li, Xinwei Fan, Jiahao Hao, Yaomin Dai, Zhiwei Wang, Yugui Yao, Hai-Hu Wen. *Origin of the Charge Density Wave in the Kagome Metal CsV3Sb5 as Revealed by Optical Spectroscopy.* Phys. Rev. B **104**, L041101 (2021).

[23] Yu-Xiao Jiang *et al. Unconventional chiral charge order in kagome superconductor KV_3Sb_5.* Nat. Mater. **20**, 1353 (2021).

[24] He Zhao, Hong Li, Brenden R. Ortiz, Samuel M. L. Teicher, Taka Park, Mengxing Ye, Ziqiang Wang, Leon Balents, Stephen D. Wilson, Ilija Zeljkovic. *Cascade of correlated electron states in a kagome superconductor CsV_3Sb_5.* Nature (2021).

[25] Zuowei Liang, Xingyuan Hou, Fan Zhang, Wanru Ma, Ping Wu, Zongyuan Zhang, Fanghang Yu, J.-J. Ying, Kun Jiang, Lei Shan, Zhenyu Wang, and X.-H. Chen. *Three-Dimensional Charge Density Wave and Surface-Dependent Vortex-Core States in a Kagome Superconductor CsV_3Sb_5.* Phys. Rev. X **11**, 031026 (2021).

[26] Hui Chen, Haitao Yang, Bin Hu, Zhen Zhao, Jie Yuan, Yuqing Xing, Guojian Qian, Zihao Huang, Geng Li, Yuhan Ye, Qiangwei Yin, Chunsheng Gong, Zhijun Tu, Hechang Lei, Shen Ma, Hua Zhang, Shunli Ni, Hengxin Tan, Chengmin Shen, Xiaoli Dong, Binghai Yan, Ziqiang Wang, and Hong-Jun Gao. *Roton pair density wave in a strong-coupling kagome superconductor.* Nature (2021).

[27] H. X. Li, T. T. Zhang, Y.-Y. Pai, C. Marvinney, A. Said, T. Yilmaz, Q. Yin, C. Gong, Z. Tu, E. Vescovo, R. G. Moore, S. Murakami, H. C. Lei, H. N. Lee, B. Lawrie, and H. Miao. *Observation of Unconventional Charge Density Wave without Acoustic Phonon Anomaly in Kagome Superconductors AV3Sb5 (A=Rb,Cs).* Phys. Rev. X **11**, 031050 (2021).

[28] Brenden R. Ortiz, Samuel M. L. Teicher, Linus Kautzsch, Paul M. Sarte, Jacob P. C. Ruff, Ram Seshadri, and Stephen D. Wilson. *Fermi surface mapping and the nature of charge density wave order in the kagome superconductor CsV_3Sb_5.* arXiv:2104.07230 (2021).

[29] Yang Luo, Shuting Peng, Samuel M. L. Teicher, Linwei Huai, Yong Hu, Brenden R. Ortiz, Zhiyuan Wei, Jianchang Shen, Zhipeng Ou, Bingqian Wang, Yu Miao, Mingyao Guo, M. Shi, Stephen D. Wilson, J.-F. He. *Distinct band reconstructions in kagome superconductor CsV3Sb.* arXiv:2106.01248 (2021).

[30] T. Qian, M. H. Christensen, C. Hu, A. Saha, B. M. Andersen, R. M. Fernandes, T. Birol, and N. Ni. *Revealing the competition between charge-density wave and superconductivity in CsV_3Sb_5 through uniaxial strain.* arXiv:2107.04545 (2021).

[31] Hong Li, He Zhao, Brenden R. Ortiz, Takamori Park, Mengxing Ye, Leon Balents, Ziqiang Wang, Stephen D. Wilson, Ilija Zeljkovic. *Rotation symmetry breaking in the normal state of a kagome superconductor KV3Sb5.* arXiv:2104.08209 (2021).

[32] Hengxin Tan, Yizhou Liu, Ziqiang Wang, Binghai Yan. *Charge density waves and electronic properties of superconducting kagome metals.* Phys. Rev. Lett. **127**, 046401 (2021).

[33] Noah Ratcliff, Lily Hallett, Brenden R. Ortiz, Stephen D. Wilson, and John W. Harter. *Coherent phonon spectroscopy and interlayer modulation of charge density wave order in the kagome metal CsV_3Sb_5.* arXiv:2104.10138 (2021).

[34] Nana Shumiya, Md Shafayat Hossain, Jia-Xin Yin, Yu-Xiao Jiang, Brenden R. Ortiz, Hongxiong Liu, Youguo Shi, Qiangwei Yin, Hechang Lei, Songtian S. Zhang, Guoqing Chang, Qi Zhang, Tyler A. Cochran, Daniel Multer, Maksim Litskevich, Zi-Jia Cheng, Xian P. Yang, Zurab Guguchia, Stephen D. Wilson, and M. Zahid Hasan. *Intrinsic nature of chiral charge order in the kagome superconductor RbV_3Sb_5.* Phys. Rev. B **104**, 035131 (2021).

[35] Yu-Ping Lin and Rahul M. Nandkishore. *Complex charge density waves at Van Hove singularity on hexagonal lattices: Haldane-model phase diagram and potential realization in the kagome metals AV_3Sb_5 (A=K, Rb, Cs).* Phys. Rev. B **104**, 045122 (2021).

[36] M. Michael Denner, Ronny Thomale, and Titus Neupert. *Analysis of charge order in the kagome metal AV_3Sb_5 (A=K,Rb,Cs).* arXiv:2103.14045 (2021).

[37] Chandan Setty, Haoyu Hu, Lei Chen, and Qimiao Si. *Electron correlations and T-breaking density wave order in a $\mathbb{Z}_2$ kagome metal.* arXiv:2105.15204 (2021).

[38] C. Mielke III, D. Das, J.-X. Yin, H. Liu, R. Gupta, C.N. Wang, Y.-X. Jiang, M. Medarde, X. Wu, H.C. Lei, J.J. Chang, P. Dai, Q. Si, H. Miao, R. Thomale, T. Neupert, Y. Shi, R. Khasanov, M.Z. Hasan, H. Luetkens, and Z. Guguchia. *Time-reversal symmetry-breaking charge order in a correlated kagome superconductor.* arXiv:2106.13443 (2021).

[39] Takamori Park, Mengxing Ye, Leon Balents. *Electronic instabilities of kagome metals: saddle points and Landau theory.* Phys. Rev. B **104**, 035142 (2021).

[40] G. Kresse and J. Hafner. *Ab initio molecular dynamics for liquid metals.* Phys. Rev. B **47**, 558(R) (1993).

[41] G. Kresse, J. Furthmüller. *Efficiency of ab-initio total energy calculations for metals and semiconductors using a plane-wave basis set.* Comp. Mat. Sci. **6**, 15 (1996).

[42] G. Kresse and J. Furthmüller. *Efficient iterative schemes for ab initio total-energy calculations using a plane-wave basis set.* Phys. Rev. B **54**, 11169 (1996).

[43] John P. Perdew, Adrienn Ruzsinszky, Gábor I. Csonka, Oleg A. Vydrov, Gustavo E. Scuseria, Lucian A. Constantin, Xiaolan Zhou, and Kieron Burke. *Restoring the Density-Gradient Expansion for Exchange in Solids and Surfaces.* Phys. Rev. Lett. **100**, 136406 (2008).

[44] Soohyun Cho, Haiyang Ma, Wei Xia, Yichen Yang, Zhengtai Liu, Zhe Huang, Zhicheng Jiang, Xiangle Lu, Jishan Liu, Zhonghao Liu, Jinfeng Jia, Yanfeng Guo, Jianpeng Liu, and Dawei Shen. *Emergence of new van Hove singularities in the charge density wave state of a topological kagome metal RbV_3Sb_5.* arXiv:2105.05117 (2021).

[45] Mingu Kang, Shiang Fang, Jeong-Kyu Kim, Brenden R. Ortiz, Jonggyu Yoo, Byeong-Gyu Park, Stephen D. Wilson, Jae-Hoon Park, and Riccardo Comin. *Twofold van Hove singularity and origin of charge order in topological kagome superconductor CsV_3Sb_5*. arXiv:2105.01689 (2021).

[46] Yong Hu, Xianxin Wu, Brenden R. Ortiz, Sailong Ju, Xinlong Han, J. Z. Ma, N. C. Plumb, Milan Radovic, Ronny Thomale, S. D. Wilson, Andreas P. Schnyder, and M. Shi. *Rich Nature of Van Hove Singularities in Kagome Superconductor CsV_3Sb_5*. arXiv:2106.05922 (2021).

[47] D. M. Hatch and H. T. Stokes. *INVARIANTS: program for obtaining a list of invariant polynomials of the order-parameter components associated with irreducible representations of a space group*. J. Appl. Cryst. **36**, 951 (2003).

[48] Pierre Toledano, and Jean-Claude Toledano. *Landau Theory Of Phase Transitions, The: Application To Structural, Incommensurate, Magnetic And Liquid Crystal Systems*. World Scientific Publishing Company (1987).

[49] Eric Bousquet, Matthew Dawber, Nicolas Stucki, Céline Lichtensteiger, Patrick Hermet, Stefano Gariglio, Jean-Marc Triscone, and Philippe Ghosez. *Improper ferroelectricity in perovskite oxide artificial superlattices*. Nature **452**, 732 (2008).

[50] Nicole A. Benedek and Craig J. Fennie. *Hybrid Improper Ferroelectricity: A Mechanism for Controllable Polarization-Magnetization Coupling*. Phys. Rev. Lett. **106**, 107204 (2011).

[51] I. Etxebarria, J. M. Perez-Mato, and P. Boullay. *The Role of Trilinear Couplings in the Phase Transitions of Aurivillius Compounds*. Ferroelectrics **401**, 17 (2010).

[52] Y. Wang and A. Chubukov. *Charge-density-wave order with momentum $(2Q, 0)$ and $(0, 2Q)$ within the spin-fermion model: Continuous and discrete symmetry breaking, preemptive composite order, and relation to pseudogap in hole-doped cuprates*. Phys. Rev. B **90**, 035149 (2014).

[53] M. Hecker and J. Schmalian. *Vestigial nematic order and superconductivity in the doped topological insulator $Cu_xBi_2Se_3$*. npj Quant. Mat. **3**, 26 (2018).

[54] R. M. Fernandes and J. W. F. Venderbos. *Nematicity with a twist: Rotational symmetry breaking in a moiré superlattice*. Sci. Adv. **6**, eaba8834 (2020).

[55] In other words, the matrices for the two irreducible representations of the space and the point groups are the same, except for the translational symmetry elements, which do not exist in the point group.

[56] R. M. Fernandes, P. P. Orth, and J. Schmalian. *Intertwined Vestigial Order in Quantum Materials: Nematicity and Beyond*. Ann. Rev. Cond. Mat. Phys. **10**, 133 (2019).

[57] C. Eckberg *et al. Sixfold enhancement of superconductivity in a tunable electronic nematic system*. Nat. Phys. **16**, 346 (2020).